Safe Operational Envelope for the LSMS Family of Cable-Driven Cranes

Javier Puig-Navarro*
Analytical Mechanics Associates, Hampton, VA, 23666, USA

Dominic Bisio†, Amelia Scott‡, Julia Cline§, and Danette Allen¶
NASA Langley Research Center, Hampton, VA, 23666, USA

The Lightweight Surface Manipulation System, or LSMS, is a family of long-reach cable-actuated robotic cranes. These cranes are designed for planetary surface operations on the Moon and Mars. Their low structural weight and compactness reduce the fuel costs associated with space travel. The LSMS can be operated by humans, remotely or on site, or autonomously. The goal of this research is to help human operators and path planning algorithms avoid unsafe states during operation. To this end, this work leverages a geometrical model of the LSMS and formulates a new dynamic model. These are used to define the safe operational envelope for the LSMS family. The paper classifies the constraints that define the safe operational envelope in three groups: motor constraints, geometric constraints, and cable tension constraints. Keeping the cables under tension is necessary to maintain controllability over the joint angles. Two types of loss of tension events are identified for each of the cables. First, an excessive reel out of the cables can lead to a loss of tension, where the LSMS links behave like a pendulum. Second, an excessive reel in of the cables can lead to a link tip-over. This can cause a violent clash between the links on the LSMS and damage the equipment. The paper visualizes these constraints for the LSMS-L35, the smallest robot within the family.

I. Nomenclature

$\{i\}$	=	ith reference frame
θ_i	=	angle for the ith joint with $i \in \{0, 1, 2\}$
$\bar{\theta}_i$	=	maximum angle for the ith joint with $i \in \{0, 1, 2\}$
$\underline{\theta}_i$	=	minimum angle for the ith joint with $i \in \{0, 1, 2\}$
$\boldsymbol{\theta}$	=	vector of joint angles
θ_X	=	fixed angle on the LSMS with $X \in \{A, B, D, E, F_1, F_2, H, I, J\}$
θ_{d_i}	=	desired angle for the ith joint with $i \in \{0, 1, 2\}$
$\dot{\theta}_{d_i}$	=	desired rate for the ith joint with $i \in \{0, 1, 2\}$
$\ddot{\theta}_{d_i}$	=	desired acceleration for the ith joint with $i \in \{0, 1, 2\}$
$\boldsymbol{\theta_d}$	=	vector of desired joint angles
$\dot{\boldsymbol{\theta}}_{\boldsymbol{d}}$	=	vector of desired joint rates
$\ddot{\boldsymbol{\theta}}_{\boldsymbol{d}}$	=	vector of desired joint accelerations
d_{XY}	=	fixed distance between relevant points X and Y
ℓ_{XY}	=	length of the cable segment between points X and Y
ω_i	=	speed of the ith motor before the gearbox with $i \in \{0, A, B\}$
$\bar{\omega}_i$	=	maximum speed for the ith motor before the gearbox with $i \in \{0, A, B\}$
$\boldsymbol{\omega}$	=	vector of motor speeds before the gearbox
$\boldsymbol{R}_i^j$	=	rotation matrix from frame $\{i\}$ to frame $\{j\}$
${}^j\boldsymbol{\omega}_i$	=	angular speed of the ith link with respect to frame $\{j\}$

*Aerospace Engineer Senior, Analytical Mechanics Associates, resident at NASA Langley Research Center, AIAA Senior Member.
†Robotics and Automated Systems Research Engineer, Autonomous Integrated Systems Research Branch, 1 NASA Drive, MS 152.
‡Research Computer Scientist, Autonomous Integrated Systems Research Branch, 1 NASA Drive, MS 152.
§Research Aerospace Engineer, Structural Mechanics and Concepts Branch, 1 NASA Drive, MS 190, AIAA Senior Member.
¶Senior Leader for Autonomous Systems and Autonomous Systems Capability Lead, NASA, AIAA Associate Fellow.

$^j\boldsymbol{\alpha}_i$ = angular acceleration of the ith link with respect to frame $\{j\}$
$^j\boldsymbol{\rho}_i$ = position of the center of mass of the ith link with respect to frame $\{j\}$
$^j\boldsymbol{v}_i$ = velocity of the center of mass of the ith link with respect to frame $\{j\}$
$^j\boldsymbol{a}_i$ = acceleration of the center of mass of the ith link with respect to frame $\{j\}$
m_i = mass of the ith link with $i \in \{0, 1, 2\}$
$^j\boldsymbol{I}_i$ = matrix of inertia of the ith link expressed in frame $\{j\}$
$^i\boldsymbol{\eta}_i$ = vector between successive reference frames $\{i\}$ and $\{i+1\}$ with $i \in \{0, 1, 2\}$
η_i = efficiency of the ith gearbox with $i \in \{0, A, B\}$
T = kinetic energy of the LSMS
T_t = contribution to the kinetic energy of the LSMS due to translations
T_r = contribution to the kinetic energy of the LSMS due to rotations
V = potential energy of the LSMS
$\boldsymbol{e_z}$ = unit vector aligned with the z axis of the ground frame
$\boldsymbol{I}$ = generalized inertia matrix
$\boldsymbol{C}$ = generalized Coriolis matrix
$\boldsymbol{\tau_g}$ = generalized forces due to gravity
$\boldsymbol{\tau_d}$ = generalized dissipation forces
$\boldsymbol{J_X}$ = Jacobian matrix for point X with $X \in \{G, K\}$
$^i\boldsymbol{w}_X$ = wrench applied at point X expressed in frame $\{i\}$ with $X \in \{G, K\}$
$\boldsymbol{B}$ = control matrix in the dynamics of the LSMS
τ_{m_i} = motor torque before the gearbox with $i \in \{0, A, B\}$
$\bar{\tau}_{m_i}$ = maximum torque before the gearbox for the ith motor with $i \in \{0, A, B\}$
$\underline{\tau}_{m_i}$ = minimum torque before the gearbox for the ith motor to maintain tension on cables with $i \in \{A, B\}$
$\boldsymbol{\tau_m}$ = vector of motor torques before the gearbox

II. Introduction

The Lightweight Surface Manipulation System, or LSMS, is a family of long-reach cable-actuated robotic cranes. Their design is particularly suited for a multitude of tasks on the surface of the Moon and Mars. Equipped with different end effectors, the LSMS can load and offload payloads from a lander [1], aid in the construction of infrastructure [2], lower instruments to lava tubes and craters, scoop regolith [3], and even weld [4]. These cranes can handle relatively heavy payloads compared to their structural mass. They also fold for space travel and self deploy once they arrive at their destination. The high payload ratio, compactness, and manipulation capabilities of the LSMS family make it a cost-effective solution for planetary surface operations. The smallest robot within the family is the LSMS-L35, illustrated in Figure 1. It has a 35 kg lift capacity on the Moon, 6 kg on Earth, and is designed for the Commercial Lunar Payload Services (CLPS) landers [5]. The largest crane is the LSMS-1000, with a 1000 kg lift capacity on the Moon, 165 kg on Earth. This version is sized for the larger Blue Moon Lander [6].

The cables in the LSMS, and the triangular pattern they form in Figure 1, are an efficient mechanism to distribute the loads along the structure. This reduces the size and mass of its links and actuators, reducing the transportation costs. However, this comes with added challenges. First, the cables cannot operate under compression and must maintain tension at all times for safe operations. Second, unlike most serial manipulators [7] where the actuators are located at the joints to be controlled, the actuators for the shoulder and elbow joints are located on the base of the LSMS, see Figure 1. As a result, mapping motor movements to joint movements is more complex, as the cable geometry must be involved, making this a nonlinear problem. Moreover, the spreaders shown in Figure 1 create a set of discrete switches in the geometry of the cables, as the spreaders rest on and separate from the cables, making this a hybrid problem as well. These properties make the definition of the safe operational envelope a challenge. Its definition, however, is of importance to define safe procedures for this type of robotic cranes.

To safely operate the LSMS a trajectory that respects the physical limitations of the crane must be provided. This trajectory can be specified by a human operator, remotely or on site, or by a kynodynamic path planner [8] in the event of autonomous operations. Regardless of the origin of this trajectory, the goal of this research is to avoid unsafe states during operation.

The contributions of the paper are threefold. First, the formulation of a dynamic model of the LSMS that computes cable forces and the corresponding motor torques under different gravity and load environments. Second, the definition and classification the constraints that describe the physical limits of the LSMS in three categories: i) motor constraints,

characterized by their maximum speeds and torques; *ii*) geometric constraints, guaranteeing that the triangle pattern shown in Figure 1 among cables, spreaders, and links is maintained and excessively slender triangles are avoided; and *iii*) the cable tension constraints, ensuring that cables are not subject to compression loads, maintaining controllability over the shoulder and elbow angles. Last, this work visualizes the safe operational envelope for the LSMS-L35, identifying the type of loss of tension events that each of its boundaries lead to.

The paper is structured as follows. Section III provides an overview of the geometric model that relates cable movements to joint rotations, originally developed in [9]. Section IV formulates a dynamic model for the LSMS family, along with the necessary forces and torques. Section V leverages these geometric and dynamic models to define and visualize the safe operational envelope. Finally, Section VI provides an overview of the physical phenomena that define the safe operational envelope of the LSMS and a summary of the severity of the different types of excursions outside of the envelope.

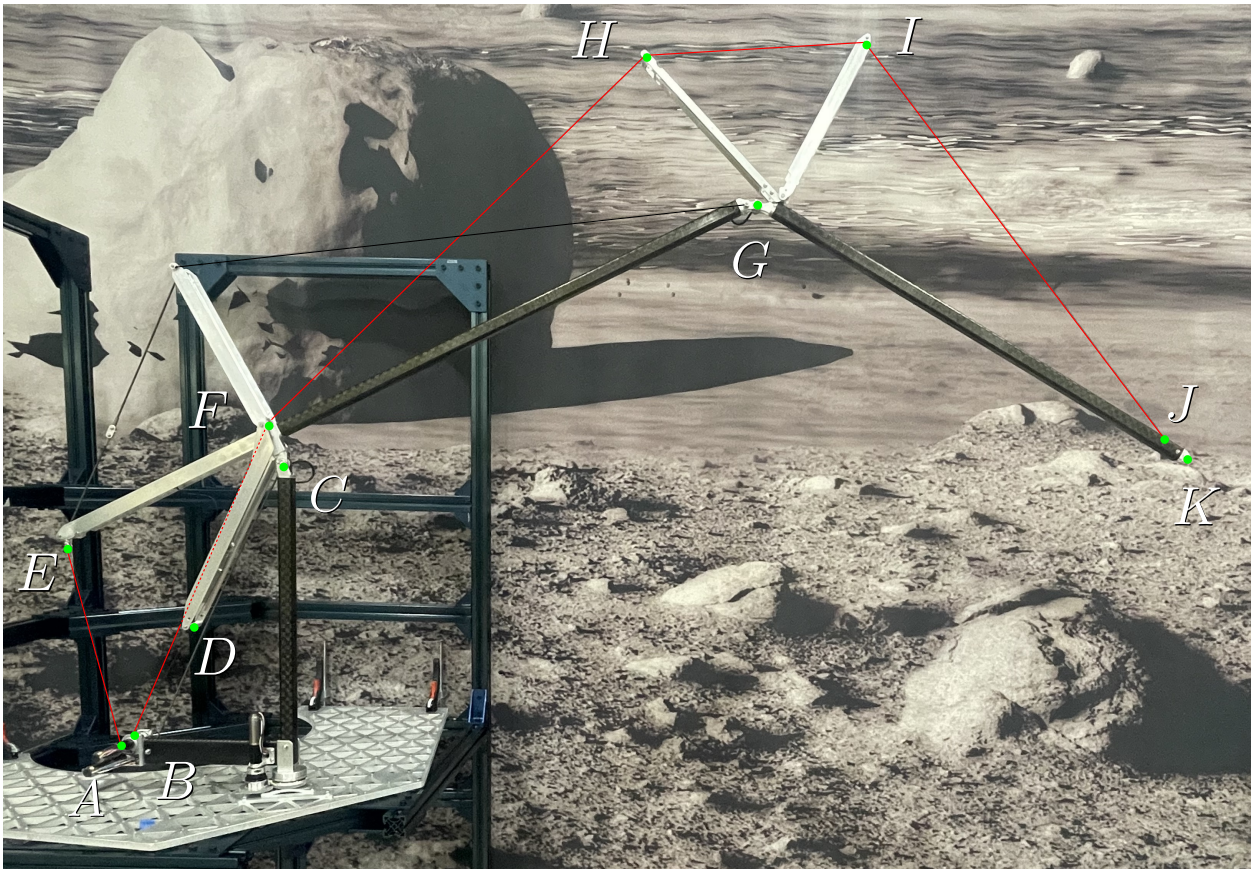
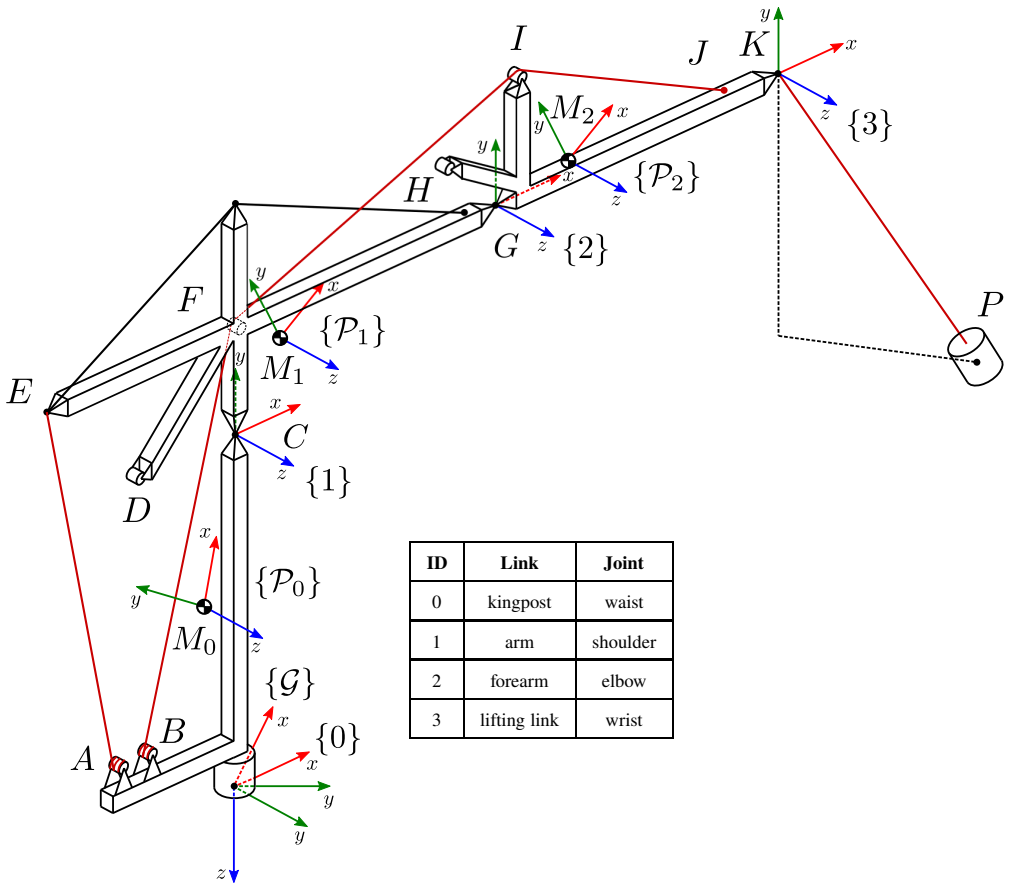


Fig. 1 The LSMS-L35 on a mock-up of the payload deck of a lunar lander [5], placed in front of a backdrop that resembles lunar terrain. Actuated cables are highlighted in red, while the cables that reinforce the structure of the LSMS are shown in black. The important points on the LSMS are marked with capital letters, and their precise location is depicted with a small green dot: A and B denote the location of the shoulder and elbow motors with their gearboxes and spools; C and G define the shoulder and elbow joints; F marks the location of a pulley embedded in the arm used to route cable B; E and J highlight the attachment points for cables A and B, respectively; K denotes the position of the wrist of the LSMS; and D, H and I point the location of small pulleys located at the end of the spreaders. These spreaders have three purposes: *i*) the efficient distribution of the loads under a wide range of shoulder and elbow angles; *ii*) managing the cable geometry to maintain the triangular pattern; and *iii*) extending the safe operational envelope of the LSMS. As the shoulder and elbow angles change, spreaders D, H, and I rest on and separate from the cables, changing the spreader configuration.



ID	Link	Joint
0	kingpost	waist
1	arm	shoulder
2	forearm	elbow
3	lifting link	wrist

Fig. 2 Schematic representing the three links and three rotational joints of the LSMS. The names and identifying numbers of the links and joints are given in the legend. Actuated cables are highlighted in red. Relevant points on the structure, like the location of routing pulley F or the pulley at the end of the spreader D, are denoted by capital letters. Reference frames are labeled using curly brackets, such as $\{0\}$, and the centers of mass of the three links are marked with the symbol ◔.

III. Geometric Model of the LSMS

Figure 2 defines the reference points and frames used to derive the geometric model of the LSMS. All passive structural components are highlighted in black, whereas moving cables are depicted in red. Cable A is attached to the arm at point E, and actuated by motor A. This motor has a gearbox with gear ratio i_A and a spool drum with radius r_A. Cable B is attached to the forearm at point J, routed through a pulley at point F, and actuated by motor B. This motor has a gearbox with gear ratio i_B and a spool drum with radius r_B. Motors A and B, their gearboxes, and spool drums are located at the base of the LSMS, which rotates with the kingpost. A third motor controls the kingpost. This motor also has a gearbox with gear ratio i_0. The angular speeds before the gearbox of the three motors that control the motion of the LSMS are $\boldsymbol{\omega} \coloneqq [\omega_0, \omega_A, \omega_B]^\top$.

All reference frames in Figure 2 are color coded, using red, green, and blue for the $\boldsymbol{x}$, $\boldsymbol{y}$ and $\boldsymbol{z}$ axes, respectively. Notice each joint of the LSMS has a reference frame that only rotates about its $\boldsymbol{z}$ axis. The four reference frames of importance for the geometric model are:

i) The ground frame, $\{\mathcal{G}\}$, is located at the base of the kingpost and is aligned with an arbitrary axes, like the north-east-down axes or some other axes of relevance to the location where the LSMS is installed.

ii) The waist frame, $\{0\}$, is located at the same point as $\{\mathcal{G}\}$. Its $\boldsymbol{x}$ axis is aligned with the plane of the LSMS, while its $\boldsymbol{z}$ axis points downward. The $\boldsymbol{y}$ axis completes the right-handed frame. The rotation of $\{0\}$ with respect to $\{\mathcal{G}\}$ is given by angle θ_0.

iii) The shoulder frame $\{1\}$ is located at point C. Its $\boldsymbol{x}$ axis is on the plane of the LSMS. The rotation of $\{1\}$ with respect to $\{0\}$ is given by angle θ_1. The $\boldsymbol{x}$ axis is parallel to the ground frame when $\theta_1 = 0$.

iv) The elbow frame $\{2\}$ is located at point G. Its $\boldsymbol{x}$ axis is contained on the plane of the LSMS. The rotation of $\{2\}$ with respect to $\{1\}$ is given by angle θ_2. The $\boldsymbol{x}$ axis is parallel to the ground plane when $\theta_1 = \theta_2 = 0$.

The waist, shoulder, and elbow joints provide three degrees of freedoms, captured by $\boldsymbol{\theta} \coloneqq [\theta_0, \theta_1, \theta_2]^\top$, with the following transformation matrices among joint frames:

$$\boldsymbol{R}_0^{\mathcal{G}} \coloneqq \begin{bmatrix} \cos\theta_0 & -\sin\theta_0 & 0 \\ \sin\theta_0 & \cos\theta_0 & 0 \\ 0 & 0 & 1 \end{bmatrix}, \quad \boldsymbol{R}_1^0 \coloneqq \begin{bmatrix} \cos\theta_1 & -\sin\theta_1 & 0 \\ 0 & 0 & 1 \\ -\sin\theta_1 & -\cos\theta_1 & 0 \end{bmatrix}, \quad \boldsymbol{R}_2^1 \coloneqq \begin{bmatrix} \cos\theta_2 & -\sin\theta_2 & 0 \\ \sin\theta_2 & \cos\theta_2 & 0 \\ 0 & 0 & 1 \end{bmatrix} \in SO(3). \tag{1}$$

Note that $\boldsymbol{R}_1^0$ is the result of two rotations: *i*) about axis $\boldsymbol{z}$ by an angle θ_1; and *ii*) about axis $\boldsymbol{x}$ by an angle of -90 degrees. The additional reference frames located at points M_0, M_1, and M_2 in Figure 2 are relevant for the dynamic model of the LSMS, and will be addressed in Section IV.

As the shoulder and elbow joints move, cables A and B may rest on or lift off from spreaders D, H, and I. Figures 3 and 4, originally published in [9], describe the geometry of the cables and are included here to aid in the description of the geometric model. Figure 3 shows the two possible spreader configurations for cable A, while Figure 4 shows the three possible spreader configurations for cable B. Based on this geometry, the authors in [9] developed a geometric model that relates the motor speeds before the gearbox to the joint rates, which is expressed here in a more compact form as follows.

$$\dot{\boldsymbol{\theta}} = \begin{bmatrix} i_0 & 0 & 0 \\ 0 & \dfrac{i_A r_A}{d_{AC} \sin\nu_A} & 0 \\ 0 & -\dfrac{i_A r_A}{d_{FG} \sin\nu_F} \dfrac{d_{BC} \sin\nu_B}{d_{AC} \sin\nu_A} & \dfrac{i_B r_B}{d_{FG} \sin\nu_F} \end{bmatrix} \boldsymbol{\omega}, \tag{2}$$

with lever angles ν_A, ν_B, and ν_F, shown in Figures 3 and 4, and defined piecewise depending on the spreader configurations as

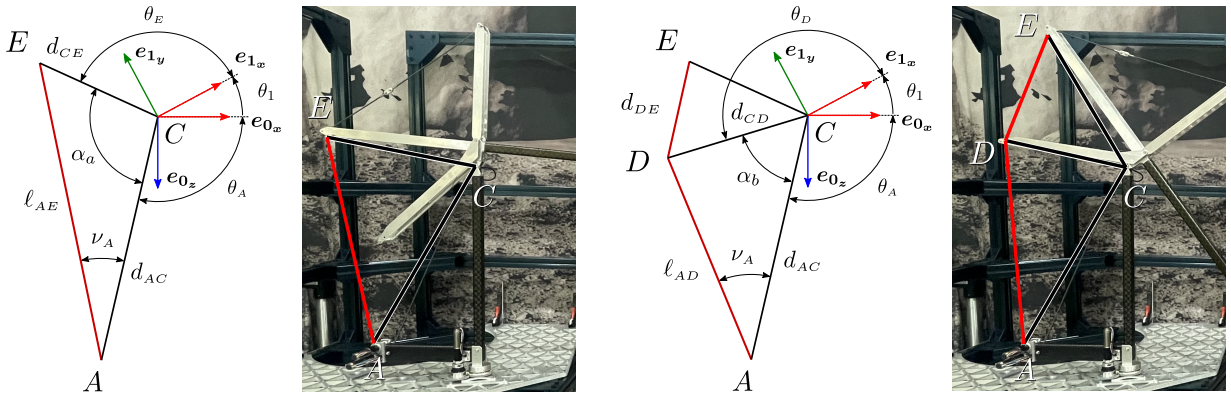
$$\sin\nu_A \coloneqq \begin{cases} \dfrac{d_{CE} \sin\alpha_a}{\ell_{AE}}, & \text{if } \theta_1 \geq \theta_1^*, \\ \dfrac{d_{CD} \sin\alpha_b}{\ell_{AD}}, & \text{if } \theta_1 < \theta_1^*, \end{cases} \quad \sin\nu_B \coloneqq \frac{d_{CF} \sin\gamma}{\ell_{BF}}, \quad \sin\nu_F \coloneqq \begin{cases} \dfrac{d_{GJ} \sin\beta_a}{\ell_{FJ}}, & \text{if } \theta_2 \geq \theta_2^*, \\ \dfrac{d_{GI} \sin\beta_b}{\ell_{FI}}, & \text{if } \theta_2^{**} \leq \theta_2 < \theta_2^*, \\ \dfrac{d_{GH} \sin\beta_c}{\ell_{FH}}, & \text{if } \theta_2 < \theta_2^{**}, \end{cases} \tag{3}$$

where θ_1^* is the transition angle between spreader configurations (a) and (b) in Figures 3a and 3b; angle θ_2^* is the transition angle between configurations (a) and (b) in Figures 4a and 4b; and θ_2^{**} is the transition angle between configurations (b) and (c) in Figures 4b and 4c. The values for these transition angles on the LSMS-L35 are shown in Table 2, along with the corresponding cable and spreader. See [9] for details regarding the computation of these transition angles. Fixed distances d_{XY} between relevant points X and Y in Equations (2) and (3) are defined in Figures 3 and 4. Angles α_a and α_b are shown in Figure 3, while angles β_a, β_b, β_c, and γ are depicted in Figure 4, and are defined as

$$\begin{aligned} \alpha_a(\theta_1) &\coloneqq 2\pi - \theta_A - \theta_E - \theta_1, & \beta_a(\theta_2) &\coloneqq 2\pi - \theta_{F_2} - \theta_J - \theta_2, \\ \alpha_b(\theta_1) &\coloneqq 2\pi - \theta_A - \theta_D - \theta_1, & \beta_b(\theta_2) &\coloneqq 2\pi - \theta_{F_2} - \theta_I - \theta_2, \\ \gamma(\theta_1) &\coloneqq 2\pi - \theta_B - \theta_{F_1} - \theta_1, & \beta_c(\theta_2) &\coloneqq 2\pi - \theta_{F_2} - \theta_H - \theta_2, \end{aligned} \tag{4}$$

where θ_A, θ_B, θ_D, θ_E, θ_{F_1}, θ_{F_2}, θ_H, θ_I and θ_J are fixed angles of the structure of the LSMS, defined in Figures 3 and 4. Last, the length ℓ_{XY} of the cable segments between points X and Y that appear in Equations (2) and (3) can be computed using the law of cosines with the following expressions:

$$\begin{aligned} \ell_{AE}^2(\theta_1) &= d_{AC}^2 + d_{CE}^2 - 2\, d_{AC}\, d_{CE} \cos\alpha_a(\theta_1), & \ell_{FJ}^2(\theta_2) &= d_{FG}^2 + d_{GJ}^2 - 2\, d_{FG}\, d_{GJ} \cos\beta_a(\theta_2), \\ \ell_{AD}^2(\theta_1) &= d_{AC}^2 + d_{CD}^2 - 2\, d_{AC}\, d_{CD} \cos\alpha_b(\theta_1), & \ell_{FI}^2(\theta_2) &= d_{FG}^2 + d_{GI}^2 - 2\, d_{FG}\, d_{GI} \cos\beta_b(\theta_2), \\ \ell_{BF}^2(\theta_1) &= d_{BC}^2 + d_{CF}^2 - 2\, d_{BC}\, d_{CF} \cos\gamma(\theta_1), & \ell_{FH}^2(\theta_2) &= d_{FG}^2 + d_{GH}^2 - 2\, d_{FG}\, d_{GH} \cos\beta_c(\theta_2). \end{aligned} \tag{5}$$

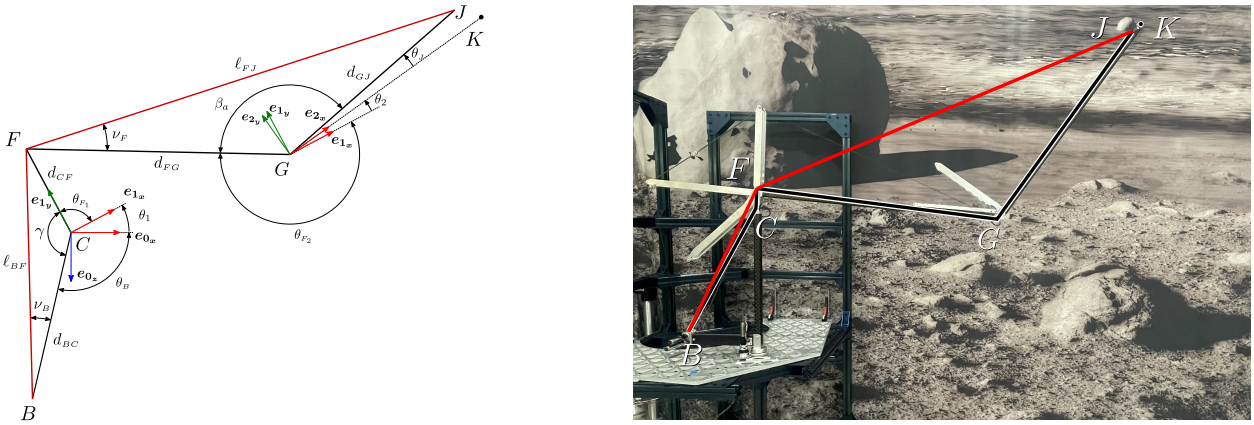


(a) Cable A does not rest against pulley D when $\theta_1 \geq \theta_1^*$. **(b) Cable A rests against pulley D when $\theta_1 < \theta_1^*$.**

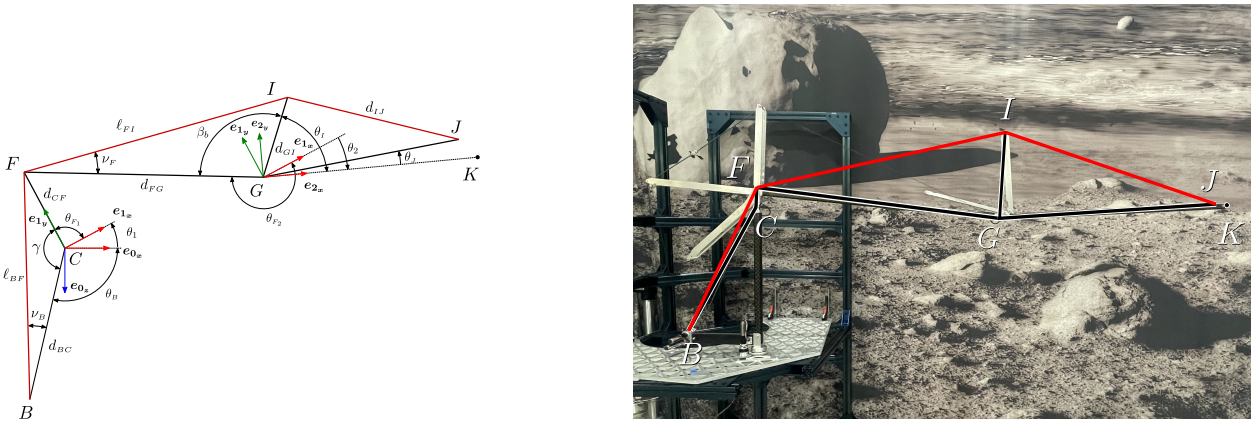
Fig. 3 Geometry of cable A [9]. The schematics show relevant parameters in the geometric model, Equation (2). The photos shows a simplified version of these schematics overlaid on a picture of the LSMS-L35. Only the kingpost and part of the arm are shown in these images. The black segments in these diagrams do not depict the struts of the LSMS, but vectors between two relevant points on the same link.

Table 2 Transition angles for the cable geometry of the LSMS-L35.

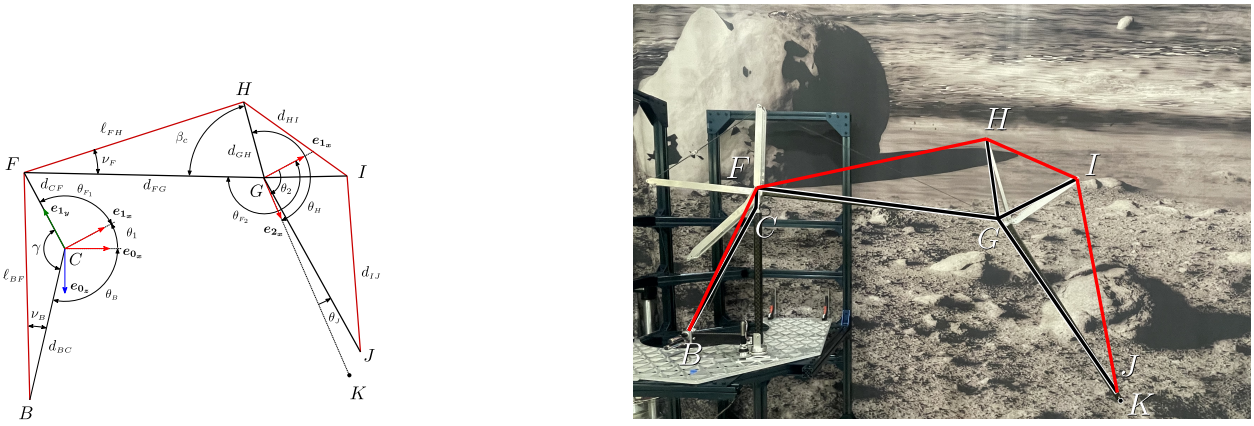
Cable	**Transition angles**	**Value** [deg]	**Spreader contact**
A	θ_1^*	−26.07	D
B	θ_2^*	38.93	I
	θ_2^{**}	−31.26	H



(a) Cable B only rests against pulley F when $\theta_2 \geq \theta_2^*$.



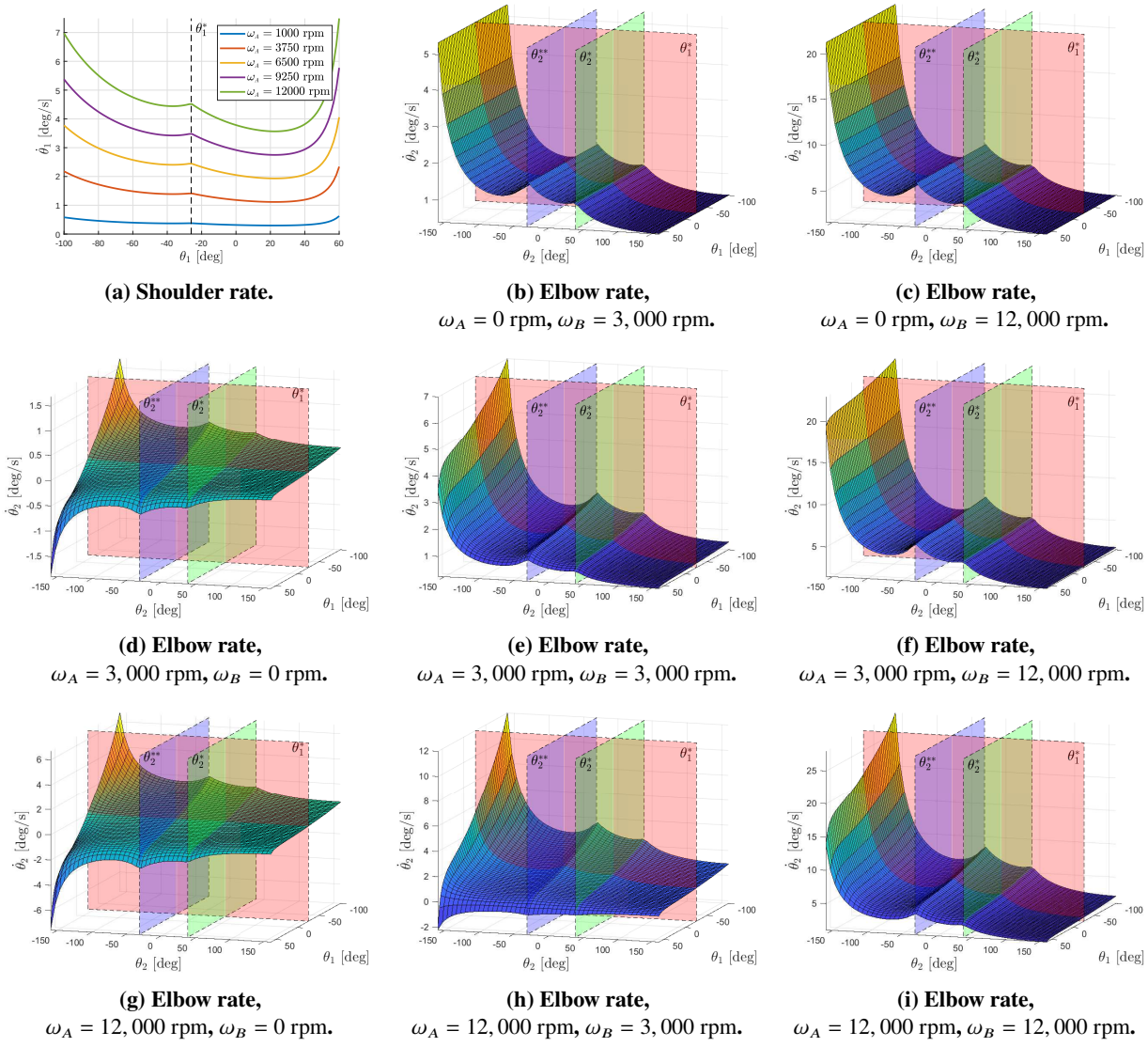
(b) Cable B rests against pulleys F and I when $\theta_2^{**} \leq \theta_2 < \theta_2^*$.



(c) Cable B rests against pulleys F, H and I when $\theta_2 < \theta_2^{**}$.

Fig. 4 Geometry of cable B [9]. The left column shows schematics with relevant parameters in the geometric model, Equation (2). The right column shows a simplified version of these schematics overlaid on a picture of the LSMS-L35. Some angles and distances in the schematics have been exaggerated for clarity.

To avoid singularities in Equation (2), the terms $\sin \nu_A$ and $\sin \nu_F$ must be bounded away from the origin. The effects of these singularities on the shoulder and elbow rates are illustrated in Figure 5, note the behavior of $\dot{\theta}_1$ at extreme values of θ_1 in Figure 5a, and the behavior of $\dot{\theta}_2$ at extreme values of θ_1 and θ_2 in Figures 5c through 5i. Note also that these surfaces are continuous but not differentiable at θ_1^*, θ_2^*, and θ_2^{**}, highlighted by the vertical dashed line in Figure 5a and by vertical planes in the remaining subfigures. The design of the safe operational envelope, in Section V, prevents the LSMS from venturing into areas of the state space that approach the singularities in Equation (2). This occurs when some of the triangles shown in Figures 3 and 4 are ill defined and either $\sin \nu_A \to 0$ or $\sin \nu_F \to 0$.



(a) Shoulder rate.

(b) Elbow rate, $\omega_A = 0$ rpm, $\omega_B = 3,000$ rpm.

(c) Elbow rate, $\omega_A = 0$ rpm, $\omega_B = 12,000$ rpm.

(d) Elbow rate, $\omega_A = 3,000$ rpm, $\omega_B = 0$ rpm.

(e) Elbow rate, $\omega_A = 3,000$ rpm, $\omega_B = 3,000$ rpm.

(f) Elbow rate, $\omega_A = 3,000$ rpm, $\omega_B = 12,000$ rpm.

(g) Elbow rate, $\omega_A = 12,000$ rpm, $\omega_B = 0$ rpm.

(h) Elbow rate, $\omega_A = 12,000$ rpm, $\omega_B = 3,000$ rpm.

(i) Elbow rate, $\omega_A = 12,000$ rpm, $\omega_B = 12,000$ rpm.

Fig. 5 Representation of the geometric model in Equation (2). The shoulder and elbow rates are shown as a function of θ_1 and θ_2 for different motor speeds, ω_A and ω_B. Figure 5a highlights the spreader transition angle θ_1^* with a vertical dashed line, while Figures 5b through 5i show the transition angles θ_1^*, θ_2^*, and θ_2^{**} with vertical planes delimited by dashed lines. Notice that the joint rates are continuous but not differentiable along these transition angles, as expected from Equation (2) and (3).

The following section complements the geometric model presented here with a dynamic model of the LSMS, to analyze relevant forces and torques.

IV. Dynamic Model of the LSMS

To model the dynamics of the LSMS, the inertial properties of the post, shoulder, and elbow are introduced: their masses m_i; the principal axes of inertia $\{\mathcal{P}_i\}$, depicted in Figure 2; their moments of inertia along the principal axis ${}^{\mathcal{P}_i}\boldsymbol{I}_i$*; the location of their centers of mass with respect to their joint frames ${}^{i}\boldsymbol{\rho}_i$; and the rotation matrices from the joint frame to the principal axes of inertia $\boldsymbol{R}_i^{\mathcal{P}_i}$ with $i \in \{0, 1, 2\}$. The centers of mass of the post, the shoulder, and the elbow are denotes in Figure 2 as M_0, M_1, and M_2, respectively. Then, *Lagrange's equation*, see [10] for further details, is used to derive the equations of motion for the LSMS

$$\frac{\mathrm{d}}{\mathrm{d}t}\left(\frac{\partial T}{\partial \dot{q}_i}\right) - \frac{\partial T}{\partial q_i} + \frac{\partial V}{\partial q_i} = Q_i, \qquad i = 0, \ldots, n-1, \tag{6}$$

where q_i is the ith generalized coordinate; n is the number of generalized coordinates; Q_i is the ith generalized force; T represents the kinetic energy and V the potential energy. To this end, select the three generalized coordinates

$$\boldsymbol{q} \coloneqq [q_0,\, q_1,\, q_2]^\top \coloneqq [\theta_0,\, \theta_1,\, \theta_2]^\top, \tag{7}$$

and compute the positions of the center of mass of each link with respect to the ground frame as

$$\begin{aligned}
{}^{\mathcal{G}}\boldsymbol{\rho}_0 &= \boldsymbol{R}_0^{\mathcal{G}0}\boldsymbol{\rho}_0, \\
{}^{\mathcal{G}}\boldsymbol{\rho}_1 &= \boldsymbol{R}_0^{\mathcal{G}}\left({}^{0}\boldsymbol{v}_{0C} + \boldsymbol{R}_1^{01}\boldsymbol{\rho}_1\right), \\
{}^{\mathcal{G}}\boldsymbol{\rho}_2 &= \boldsymbol{R}_0^{\mathcal{G}}\left({}^{0}\boldsymbol{v}_{0C} + \boldsymbol{R}_1^{0}\left({}^{1}\boldsymbol{v}_{CG} + \boldsymbol{R}_2^{12}\boldsymbol{\rho}_2\right)\right).
\end{aligned} \tag{8}$$

These expressions can be easily generalized for an arbitrary link number j

$${}^{\mathcal{G}}\boldsymbol{\rho}_j = \sum_{0}^{j-1}{}_{k} \boldsymbol{R}_k^{\mathcal{G}k}\boldsymbol{\eta}_k + \boldsymbol{R}_j^{\mathcal{G}j}\boldsymbol{\rho}_j, \tag{9}$$

where ${}^{k}\boldsymbol{\eta}_k$ is the vector that goes from reference frame $\{k\}$ to $\{k+1\}$, expressed in frame $\{k\}$. Note that in the summation above, if the upper index is smaller than the lower index then the result of the summation is $\mathbf{0}$. This applies throughout all summation limits within this text. Taking the time derivative yields the speed of the centers of mass of each of the links of the LSMS

$$\begin{aligned}
{}^{\mathcal{G}}\boldsymbol{v}_0 &= \boldsymbol{R}_0^{\mathcal{G}0}\boldsymbol{\omega}_0^{\wedge 0}\boldsymbol{\rho}_0, \\
{}^{\mathcal{G}}\boldsymbol{v}_1 &= \boldsymbol{R}_0^{\mathcal{G}0}\boldsymbol{\omega}_0^{\wedge}\left({}^{0}\boldsymbol{v}_{0C} + \boldsymbol{R}_1^{01}\boldsymbol{\rho}_1\right) + \boldsymbol{R}_0^{\mathcal{G}}\boldsymbol{R}_1^{01}\boldsymbol{\omega}_1^{\wedge 1}\boldsymbol{\rho}_1, \\
{}^{\mathcal{G}}\boldsymbol{v}_2 &= \boldsymbol{R}_0^{\mathcal{G}0}\boldsymbol{\omega}_0^{\wedge}\left({}^{0}\boldsymbol{v}_{0C} + \boldsymbol{R}_1^{0}\left({}^{1}\boldsymbol{v}_{CG} + \boldsymbol{R}_2^{12}\boldsymbol{\rho}_2\right)\right) + \boldsymbol{R}_0^{\mathcal{G}}\boldsymbol{R}_1^{01}\boldsymbol{\omega}_1^{\wedge}\left({}^{1}\boldsymbol{v}_{CG} + \boldsymbol{R}_2^{12}\boldsymbol{\rho}_2\right) + \boldsymbol{R}_0^{\mathcal{G}}\boldsymbol{R}_1^{0}\boldsymbol{R}_2^{12}\boldsymbol{\omega}_2^{\wedge 2}\boldsymbol{\rho}_2,
\end{aligned} \tag{10}$$

where $(\cdot)^\wedge$ denotes the hat map† of a vector in $\mathbb{R}^3$. Again, generalizing these expressions for an arbitrary link number j leads to

$${}^{\mathcal{G}}\boldsymbol{v}_j = \sum_{0}^{j}{}_{k} \dot{\theta}_k \boldsymbol{R}_k^{\mathcal{G}}\boldsymbol{L_z}{}^{k}\boldsymbol{\rho}_j, \tag{11}$$

where $\boldsymbol{L_z}$ is the following member in the basis of SO(3):

$$\boldsymbol{L_z} \coloneqq \begin{bmatrix} 0 & -1 & 0 \\ 1 & 0 & 0 \\ 0 & 0 & 0 \end{bmatrix}, \tag{12}$$

and ${}^{k}\boldsymbol{\rho}_j$ is a generalization of Equation (9) that represents the the center of mass of the jth link with respect to the joint frame $\{k\}$, that is

$${}^{k}\boldsymbol{\rho}_j = \sum_{k}^{j-1}{}_{\ell} \boldsymbol{R}_\ell^{k\ell}\boldsymbol{\eta}_\ell + \boldsymbol{R}_j^{kj}\boldsymbol{\rho}_j, \qquad \forall k \le j. \tag{13}$$

*Since the moments of inertia are defined with respect to the principal axis, ${}^{\mathcal{P}_i}\boldsymbol{I}_i$ are diagonal matrices for all $i \in \{0, 1, 2\}$.

†Given a vector $\boldsymbol{\omega} \coloneqq [\omega_x, \omega_y, \omega_z]^\top \in \mathbb{R}^3$, the hat map is defined as

$$\boldsymbol{\omega}^\wedge \coloneqq \begin{bmatrix} 0 & -\omega_z & \omega_y \\ \omega_z & 0 & -\omega_x \\ -\omega_y & \omega_x & 0 \end{bmatrix}.$$

Taking the time derivative of the velocity vectors yields the acceleration of the centers of mass of the links

$$
\begin{aligned}
{}^{\mathcal{G}}\boldsymbol{a}_0 &= \boldsymbol{R}_0^{\mathcal{G}} \left({}^0\boldsymbol{\omega}_0^{\wedge}\right)^2 {}^0\boldsymbol{\rho}_0 + \boldsymbol{R}_0^{\mathcal{G}0} {}^0\boldsymbol{\alpha}_0^{\wedge} {}^0\boldsymbol{\rho}_0,\\
{}^{\mathcal{G}}\boldsymbol{a}_1 &= \boldsymbol{R}_0^{\mathcal{G}} \left({}^0\boldsymbol{\omega}_0^{\wedge}\right)^2 \left({}^0\boldsymbol{v}_{0C} + \boldsymbol{R}_1^{01}\boldsymbol{\rho}_1\right) + \boldsymbol{R}_0^{\mathcal{G}0} {}^0\boldsymbol{\alpha}_0^{\wedge} \left({}^0\boldsymbol{v}_{0C} + \boldsymbol{R}_1^{01}\boldsymbol{\rho}_1\right) + 2\boldsymbol{R}_0^{\mathcal{G}0} {}^0\boldsymbol{\omega}_0^{\wedge} \boldsymbol{R}_1^{01} {}^1\boldsymbol{\omega}_1^{\wedge} \boldsymbol{\rho}_1 + \boldsymbol{R}_0^{\mathcal{G}} \boldsymbol{R}_1^0 \left({}^1\boldsymbol{\omega}_1^{\wedge}\right)^2 {}^1\boldsymbol{\rho}_1 + \boldsymbol{R}_0^{\mathcal{G}} \boldsymbol{R}_1^{01} {}^1\boldsymbol{\alpha}_1^{\wedge} {}^1\boldsymbol{\rho}_1,\\
{}^{\mathcal{G}}\boldsymbol{a}_2 &= \boldsymbol{R}_0^{\mathcal{G}} \left({}^0\boldsymbol{\omega}_0^{\wedge}\right)^2 \left({}^0\boldsymbol{v}_{0C} + \boldsymbol{R}_1^0 \left({}^1\boldsymbol{v}_{CG} + \boldsymbol{R}_2^{12}\boldsymbol{\rho}_2\right)\right) + \boldsymbol{R}_0^{\mathcal{G}0} {}^0\boldsymbol{\alpha}_0^{\wedge} \left({}^0\boldsymbol{v}_{0C} + \boldsymbol{R}_1^0 \left({}^1\boldsymbol{v}_{CG} + \boldsymbol{R}_2^{12}\boldsymbol{\rho}_2\right)\right) 2\boldsymbol{R}_0^{\mathcal{G}0} {}^0\boldsymbol{\omega}_0^{\wedge} \boldsymbol{R}_1^{01} {}^1\boldsymbol{\omega}_1^{\wedge} \left({}^1\boldsymbol{v}_{CG} + \boldsymbol{R}_2^{12}\boldsymbol{\rho}_2\right) +\\
&\quad 2\boldsymbol{R}_0^{\mathcal{G}0} {}^0\boldsymbol{\omega}_0^{\wedge} \boldsymbol{R}_1^0 \boldsymbol{R}_2^{12} {}^2\boldsymbol{\omega}_2^{\wedge} \boldsymbol{\rho}_2 + \boldsymbol{R}_0^{\mathcal{G}} \boldsymbol{R}_1^0 \left({}^1\boldsymbol{\omega}_1^{\wedge}\right)^2 \left({}^1\boldsymbol{v}_{CG} + \boldsymbol{R}_2^{12}\boldsymbol{\rho}_2\right) + \boldsymbol{R}_0^{\mathcal{G}} \boldsymbol{R}_1^{01} {}^1\boldsymbol{\alpha}_1^{\wedge} \left({}^1\boldsymbol{v}_{CG} + \boldsymbol{R}_2^{12}\boldsymbol{\rho}_2\right) +\\
&\quad 2\boldsymbol{R}_0^{\mathcal{G}} \boldsymbol{R}_1^{01} {}^1\boldsymbol{\omega}_1^{\wedge} \boldsymbol{R}_2^{12} {}^2\boldsymbol{\omega}_2^{\wedge} \boldsymbol{\rho}_2 + \boldsymbol{R}_0^{\mathcal{G}} \boldsymbol{R}_1^0 \boldsymbol{R}_2^1 \left({}^2\boldsymbol{\omega}_2^{\wedge}\right)^2 {}^2\boldsymbol{\rho}_2 + \boldsymbol{R}_0^{\mathcal{G}} \boldsymbol{R}_1^0 \boldsymbol{R}_2^{12} {}^2\boldsymbol{\alpha}_2^{\wedge} \boldsymbol{\rho}_2.
\end{aligned}
\tag{14}
$$

Again, generalizing these expressions for an arbitrary link number j yields[‡]

$$
{}^{\mathcal{G}}\boldsymbol{a}_j = \sum_0^j{}_k \ddot{\theta}_k \boldsymbol{R}_k^{\mathcal{G}} \boldsymbol{L}_{\boldsymbol{z}}{}^k \boldsymbol{\rho}_j + \sum_0^j{}_k \sum_0^k{}_\ell \dot{\theta}_k \dot{\theta}_\ell \boldsymbol{R}_\ell^{\mathcal{G}} \boldsymbol{L}_{\boldsymbol{z}} \boldsymbol{R}_k^\ell \boldsymbol{L}_{\boldsymbol{z}}{}^k \boldsymbol{\rho}_j + \sum_0^{j-1}{}_k \sum_{k+1}^j{}_\ell \dot{\theta}_k \dot{\theta}_\ell \boldsymbol{R}_k^{\mathcal{G}} \boldsymbol{L}_{\boldsymbol{z}} \boldsymbol{R}_\ell^k \boldsymbol{L}_{\boldsymbol{z}}{}^\ell \boldsymbol{\rho}_j. \tag{15}
$$

Next, the angular speed of each link expressed in its principal axes as

$$
\begin{aligned}
{}^{\mathcal{P}_0}\boldsymbol{\omega}_0 &= \boldsymbol{R}_0^{\mathcal{P}_0 0} \boldsymbol{\omega}_0,\\
{}^{\mathcal{P}_1}\boldsymbol{\omega}_1 &= \boldsymbol{R}_1^{\mathcal{P}_1} \left(\boldsymbol{R}_1^{0\top 0} \boldsymbol{\omega}_0 + {}^1\boldsymbol{\omega}_1\right),\\
{}^{\mathcal{P}_2}\boldsymbol{\omega}_2 &= \boldsymbol{R}_2^{\mathcal{P}_2} \left(\boldsymbol{R}_2^{1\top} \boldsymbol{R}_1^{0\top 0} \boldsymbol{\omega}_0 + \boldsymbol{R}_2^{1\top 1} \boldsymbol{\omega}_1 + {}^2\boldsymbol{\omega}_2\right).
\end{aligned}
\tag{16}
$$

Again, generalizing these expressions for an arbitrary link number j yields

$$
{}^{\mathcal{P}_j}\boldsymbol{\omega}_j = \boldsymbol{R}_j^{\mathcal{P}_j} \sum_0^j{}_k \dot{\theta}_k \boldsymbol{R}_j^{k\top} \boldsymbol{e}_{\boldsymbol{z}}. \tag{17}
$$

Taking the time derivative yields the angular acceleration of the links

$$
\begin{aligned}
{}^{\mathcal{P}_0}\boldsymbol{\alpha}_0 &= \boldsymbol{R}_0^{\mathcal{P}_0 0} \boldsymbol{\alpha}_0,\\
{}^{\mathcal{P}_1}\boldsymbol{\alpha}_1 &= \boldsymbol{R}_1^{\mathcal{P}_1} \left(\left({}^1\boldsymbol{\omega}_1^{\wedge}\right)^\top \boldsymbol{R}_1^{0\top 0} \boldsymbol{\omega}_0\right) + \boldsymbol{R}_1^{\mathcal{P}_1} \left(\boldsymbol{R}_1^{0\top 0} \boldsymbol{\alpha}_0 + {}^1\boldsymbol{\alpha}_1\right),\\
{}^{\mathcal{P}_2}\boldsymbol{\alpha}_2 &= \boldsymbol{R}_2^{\mathcal{P}_2} \left(\left({}^2\boldsymbol{\omega}_2^{\wedge}\right)^\top \boldsymbol{R}_2^{1\top} \boldsymbol{R}_1^{0\top 0} \boldsymbol{\omega}_0 + \boldsymbol{R}_2^{1\top} \left({}^1\boldsymbol{\omega}_1^{\wedge}\right)^\top \boldsymbol{R}_1^{0\top 0} \boldsymbol{\omega}_0 + \left({}^2\boldsymbol{\omega}_2^{\wedge}\right)^\top \boldsymbol{R}_2^{1\top 1} \boldsymbol{\omega}_1\right) + \boldsymbol{R}_2^{\mathcal{P}_2} \left(\boldsymbol{R}_2^{1\top} \boldsymbol{R}_1^{0\top 0} \boldsymbol{\alpha}_0 + \boldsymbol{R}_2^{1\top 1} \boldsymbol{\alpha}_1 + {}^2\boldsymbol{\alpha}_2\right).
\end{aligned}
\tag{18}
$$

Generalizing these expressions for an arbitrary link number j yields

$$
{}^{\mathcal{P}_j}\boldsymbol{\alpha}_j = \boldsymbol{R}_j^{\mathcal{P}_j} \sum_0^j{}_k \ddot{\theta}_k \boldsymbol{R}_j^{k\top} \boldsymbol{e}_{\boldsymbol{z}} + \boldsymbol{R}_j^{\mathcal{P}_j} \sum_0^{j-1}{}_k \sum_{k+1}^j{}_\ell \dot{\theta}_k \dot{\theta}_\ell \boldsymbol{R}_j^{\ell\top} \boldsymbol{L}_{\boldsymbol{z}}^\top \boldsymbol{R}_\ell^{k\top} \boldsymbol{e}_{\boldsymbol{z}}. \tag{19}
$$

The linear and angular position, velocities, and accelerations of the links of the LSMS are all the ingredients necessary to derive the equations of motion using *Lagrange's equation*. Next, and for simplicity, separate the *kinetic energy* into two terms, rotational and translational, as follows.

$$
T = T_t + T_r. \tag{20}
$$

These can be expressed in terms of the generalized coordinates as

$$
T_t \coloneqq \frac{1}{2} \sum_0^2{}_i m_j {}^{\mathcal{G}}\boldsymbol{v}_j^{\top\,\mathcal{G}} \boldsymbol{v}_j, \qquad T_r \coloneqq \frac{1}{2} \sum_0^2{}_j {}^{\mathcal{P}_j}\boldsymbol{\omega}_j^{\top\,\mathcal{P}_j} \boldsymbol{I}_j {}^{\mathcal{P}_j}\boldsymbol{\omega}_j. \tag{21}
$$

[‡]An alternative, but equivalent, expression for the acceleration of the center of mass of the jth link, which is useful for certain operations, is

$$
{}^{\mathcal{G}}\boldsymbol{a}_j = \sum_0^j{}_k \ddot{\theta}_k \boldsymbol{R}_k^{\mathcal{G}} \boldsymbol{L}_{\boldsymbol{z}}{}^k \boldsymbol{\rho}_j + \sum_0^j{}_k \dot{\theta}_k^2 \boldsymbol{R}_k^{\mathcal{G}} \boldsymbol{L}_{\boldsymbol{z}} \boldsymbol{L}_{\boldsymbol{z}}{}^k \boldsymbol{\rho}_j + 2 \sum_0^{j-1}{}_k \sum_{k+1}^j{}_\ell \dot{\theta}_k \dot{\theta}_\ell \boldsymbol{R}_k^{\mathcal{G}} \boldsymbol{L}_{\boldsymbol{z}} \boldsymbol{R}_\ell^k \boldsymbol{L}_{\boldsymbol{z}}{}^\ell \boldsymbol{\rho}_j.
$$

To compute the *potential energy* of the LSMS, define $\boldsymbol{e_z} \coloneqq [0, 0, 1]^\top$, and use the position of the centers of mass of the post, shoulder, and elbow

$$V = g\boldsymbol{e}_z^\top \sum_0^2{}_j \, m_j{}^{\mathcal{G}}\boldsymbol{\rho}_j. \tag{22}$$

Lastly, apply Equation 6 to the kinetic and potential energies to obtain the following equation of motion for the LSMS:

$$\boldsymbol{I}(\boldsymbol{\theta})\ddot{\boldsymbol{\theta}} = -\boldsymbol{C}(\boldsymbol{\theta}, \dot{\boldsymbol{\theta}})\dot{\boldsymbol{\theta}} + \boldsymbol{\tau_g}(\boldsymbol{\theta}) + \boldsymbol{\tau_d}(\boldsymbol{\theta}, \dot{\boldsymbol{\theta}}) + \boldsymbol{J}_G^\top(\boldsymbol{\theta})^r\boldsymbol{w}_G + \boldsymbol{J}_K^\top(\boldsymbol{\theta})^s\boldsymbol{w}_K + \boldsymbol{B}(\boldsymbol{\theta})\boldsymbol{\tau_m}, \tag{23}$$

where $\boldsymbol{I}(\boldsymbol{\theta})$ is the generalized inertia matrix; $\boldsymbol{C}(\boldsymbol{\theta}, \dot{\boldsymbol{\theta}})\dot{\boldsymbol{\theta}}$ is a quadratic term that captures the Coriolis and centrifugal forces; $\boldsymbol{\tau_g}(\boldsymbol{\theta})$ are the torques due to gravity applied on each of the joints; $\boldsymbol{\tau_d}(\boldsymbol{\theta}, \dot{\boldsymbol{\theta}})$ represents the dissipation torques due to dry friction at the joints; $\boldsymbol{J}_G(\boldsymbol{\theta})$ is the Jacobian at point G, the elbow; ${}^r\boldsymbol{w}_G$ is the wrench applied by the payload at the elbow, expressed on the rth frame; $\boldsymbol{J}_K(\boldsymbol{\theta})$ is the Jacobian at point K, the attachment point for the lifting link; ${}^s\boldsymbol{w}_K$ is the wrench applied by the payload at point K, expressed in the sth frame; $\boldsymbol{B}(\boldsymbol{\theta})$ is the control matrix; and $\boldsymbol{\tau_m}$ are the active torques applied by the motors of the LSMS before the gearbox. See the Appendix for a detailed derivation of these terms. The next section leverages the geometric and dynamic models presented to define the safe operational envelope for the LSMS.

V. Definition of the Safe Operational Envelope

To control the motion of the LSMS, a sequence of desired joint angles that remains within the safe operational envelope must be provided. Either a human operator through a remote controller, or a path planning algorithm can generate these trajectories. Internally, the LSMS should accept or reject these trajectories to protect its integrity and that of the lander or vehicle it us mounted on. To this end, assume the desired trajectory $\boldsymbol{\theta_d}(t) \coloneqq [\theta_{d_0}(t), \theta_{d_1}(t), \theta_{d_2}(t)]^\top$ is time parameterized with

$$\theta_{d_i}(t) : \mathbb{R}^+ \to SO(3). \tag{24}$$

Assume that the first and second derivatives with respect to time, that is $\dot{\boldsymbol{\theta}}_{\boldsymbol{d}}(t) \coloneqq [\dot{\theta}_{d_0}(t), \dot{\theta}_{d_1}(t), \dot{\theta}_{d_2}(t)]^\top$, and $\ddot{\boldsymbol{\theta}}_{\boldsymbol{d}}(t) \coloneqq [\ddot{\theta}_{d_0}(t), \ddot{\theta}_{d_1}(t), \ddot{\theta}_{d_2}(t)]^\top$, are also available to determine whether the desired trajectory remains within the safe operational envelope of the LSMS. The following sections define the constraints that must be met to ensure the trajectory is within the safe envelope of the LSMS. The discussion begins with the motor constraints.

A. Motor Constraints

The physical limits of the motors that run the LSMS are characterized by their maximum speed and torque, $\bar{\omega}_i$ and $\bar{\tau}_i$, respectively, with $i \in \{0, A, B\}$. To ensure that the desired trajectory meets the motor speed constraints, replace the actual joint angles and rates in Equation (2) by their desired counterparts, $\boldsymbol{\theta_d}$ and $\dot{\boldsymbol{\theta}}_{\boldsymbol{d}}$, and solve for $\boldsymbol{\omega}$ to arrive at the following result:

$$\omega_0 = \frac{1}{i_0}\dot{\theta}_{d_0}, \qquad \omega_A = \frac{d_{AC}\sin\nu_A}{i_A r_A}\dot{\theta}_{d_1}, \qquad \omega_B = \frac{d_{FG}\sin\nu_F}{i_B r_B}\left(\dot{\theta}_{d_2} + \frac{d_{BC}\sin\nu_B}{d_{FG}\sin\nu_F}\dot{\theta}_{d_1}\right). \tag{25}$$

In the expressions above, ν_A and ν_B are functions of θ_{d_1}, whereas ν_F is expressed in terms of θ_{d_2}. Finally, use this result to check whether the motor speeds remain within the prescribed bounds

$$|\omega_0| \le \bar{\omega}_0, \quad |\omega_A| \le \bar{\omega}_A, \quad |\omega_B| \le \bar{\omega}_B. \tag{26}$$

The safe operational envelope for motor 0 as a function of $\dot{\theta}_0$ is trivial. For brevity, it is not depicted here. Figure 6 presents the result of evaluating Equations (25) and (26) for motor A, at different values of θ_1 and $\dot{\theta}_1$. Notice that the safe region, highlighted in green, is symmetric with respect to the x axis. The unsafe region appears at high positive and negative values of $\dot{\theta}_1$ around θ_1^*. Recall from Figure 5a that at extreme values of θ_1 the angular rate $\dot{\theta}_1$ is significantly higher than for central values of θ_1. The results in Figure 6 are consistent with Figure 5a.

Figure 7 presents the speed constraints for motor B. According to Equation (25), these depend on θ_1, θ_2, $\dot{\theta}_1$ and $\dot{\theta}_2$. Note that the effects of θ_1 and $\dot{\theta}_1$, caused by the shoulder-elbow coupling, are much smaller than those of θ_2 and $\dot{\theta}_2$. As expected, Figures 7b, 7e, and 7h are identical and symmetric with respect to the x axis, since $\dot{\theta}_1 = 0$ deg/s. However, when $\dot{\theta}_1 \neq 0$ deg/s the figures lose the symmetry with respect to the x axis, as expected from Equation (25). Compare, for example, Figures 7a and 7c and observe how the safe region shifts upward for $\dot{\theta}_1 < 0$ and $\theta_1 > 0$, and downward

for $\dot{\theta}_1 > 0$ and $\theta_1 > 0$, as expected from Equation (25). The motor specifications used in these computations consider a high reduction gear ratio $i_i = 1/850$ and a maximum motor speed before the gearbox $\bar{\omega}_i = 12,000$ rpm for all $i \in \{0, A, B\}$.

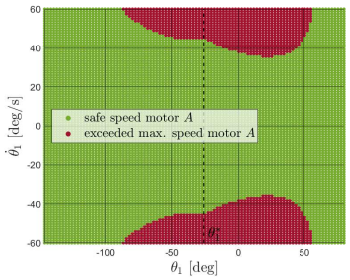
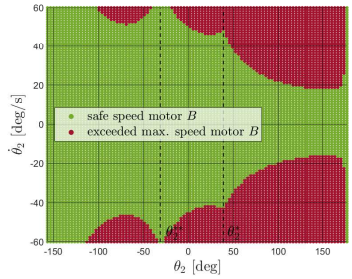
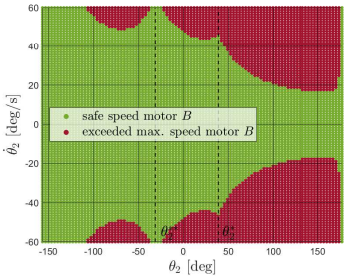


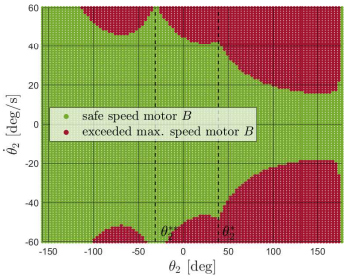
Fig. 6 Speed constraints for motor A on the LSMS-L35.



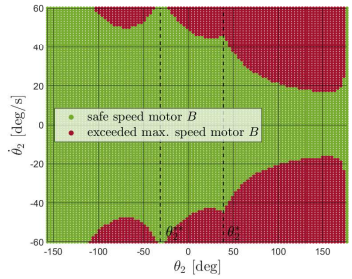
(a) $\theta_1 = 40$ deg, $\dot{\theta}_1 = -20$ deg/s.



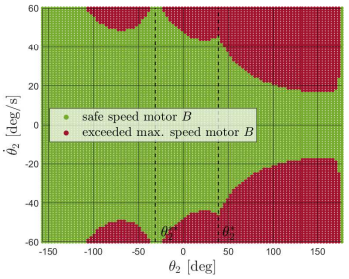
(b) $\theta_1 = 40$ deg, $\dot{\theta}_1 = 0$ deg/s.



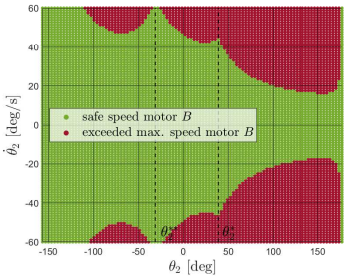
(c) $\theta_1 = 40$ deg, $\dot{\theta}_1 = 20$ deg/s.



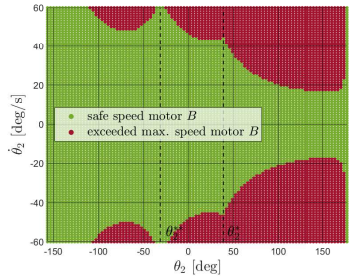
(d) $\theta_1 = 0$ deg, $\dot{\theta}_1 = -20$ deg/s.



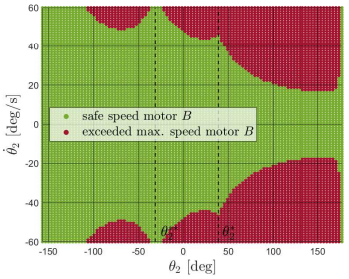
(e) $\theta_1 = 0$ deg, $\dot{\theta}_1 = 0$ deg/s.



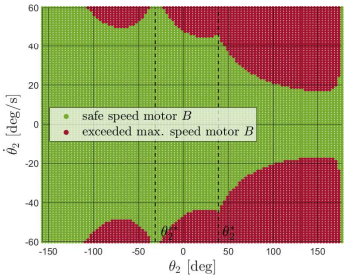
(f) $\theta_1 = 0$ deg, $\dot{\theta}_1 = 20$ deg/s.



(g) $\theta_1 = -40$ deg, $\dot{\theta}_1 = -20$ deg/s.



(h) $\theta_1 = -40$ deg, $\dot{\theta}_1 = 0$ deg/s.



(i) $\theta_1 = -40$ deg, $\dot{\theta}_1 = 20$ deg/s.

Fig. 7 Speed constraints for motor B on the LSMS-L35.

To check the motor torque constraints, replace the angles, rates, and accelerations in Equation (23) by their desired counterparts, that is $\boldsymbol{\theta_d}$, $\dot{\boldsymbol{\theta}}_{\boldsymbol{d}}$, and $\ddot{\boldsymbol{\theta}}_{\boldsymbol{d}}$, and solve for the motor torque commands

$$\boldsymbol{\tau_m} = \boldsymbol{B}^{-1}(\boldsymbol{\theta_d}) \left(\boldsymbol{I}(\boldsymbol{\theta_d})\ddot{\boldsymbol{\theta}}_{\boldsymbol{d}} + \boldsymbol{C}(\boldsymbol{\theta_d}, \dot{\boldsymbol{\theta}}_{\boldsymbol{d}})\dot{\boldsymbol{\theta}}_{\boldsymbol{d}} - \boldsymbol{\tau_g}(\boldsymbol{\theta_d}) - \boldsymbol{\tau_d}(\boldsymbol{\theta_d}, \dot{\boldsymbol{\theta}}_{\boldsymbol{d}}) - \boldsymbol{J}_G^{\top}(\boldsymbol{\theta_d})^r \boldsymbol{w}_G - \boldsymbol{J}_K^{\top}(\boldsymbol{\theta_d})^s \boldsymbol{w}_K \right). \tag{27}$$

Then, use this result to check if the motor torques remain within the prescribed bounds.

$$|\tau_{m_0}| \leq \bar{\tau}_{m_0}, \quad |\tau_{m_A}| \leq \bar{\tau}_{m_A}, \quad |\tau_{m_B}| \leq \bar{\tau}_{m_B}. \tag{28}$$

The following section addresses the constraints that arise from the geometric model of the LSMS, which was discussed in Section III.

B. Geometric Constraints

The LSMS is equipped with three encoders and three motors that are used to control its joints. All their power and data transmission cables are routed through the base of the kingpost, along the axis of rotation of the waist. To prevent excessive twisting on these cables, which could lead to their breakage, select lower and upper bounds $\underline{\theta}_0$ and $\bar{\theta}_0$, such that

$$\underline{\theta}_0 \leq \theta_{d_0} \leq \bar{\theta}_0. \tag{29}$$

Next, recall that the geometric model in Equation (2) relates the motor speeds to the joint rates. Notice that when $\sin \nu_A \to 0$ then $\dot{\theta}_1 \to \infty$. To avoid this singularity, derive safe operational bounds for the shoulder angle. To this end, define a lower bound for $\sin \nu_A \geq \zeta_A > 0$. Then, solving for ν_A in $\sin \nu_A = \zeta_A$ yields

$$\underline{\nu}_A = \arcsin \zeta_A. \tag{30}$$

To avoid excessively cropping the operational envelope of the LSMS, choose ζ_A such that $\underline{\nu}_A < \nu_A(\theta_1^*)$. This can be easily accomplished by selecting $\zeta_A < \sin \nu_A(\theta_1^*)$. Next, find the bounds on $\underline{\theta}_1$ and $\bar{\theta}_1]$ that correspond to $\underline{\nu}_A$ by solving the following equations:

$$\sin \underline{\nu}_A = \frac{d_{CE} \sin \alpha_a(\bar{\theta}_1)}{\ell_{AE}(\bar{\theta}_1)}, \qquad \sin \underline{\nu}_A = \frac{d_{CD} \sin \alpha_b(\underline{\theta}_1)}{\ell_{AD}(\underline{\theta}_1)}. \tag{31}$$

To this end, square the expressions at either side of the equalities; leverage trigonometric identities; and use the definitions of $\alpha_a(\theta_1)$ and $\alpha_b(\theta_1)$ in Equation (4), and $\ell_{AD}(\theta_1)$ and $\ell_{AE}(\theta_1)$ in Equation (5) to arrive at the following expressions:

$$\underline{\theta}_1 \coloneqq 2\pi - \theta_A - \theta_D - \bar{f}\left(\frac{d_{AC}}{d_{CD}}, \underline{\nu}_A\right), \qquad \bar{\theta}_1 \coloneqq 2\pi - \theta_A - \theta_E - \underline{f}\left(\frac{d_{AC}}{d_{CE}}, \underline{\nu}_A\right), \tag{32}$$

where functions $\bar{f}$ and $\underline{f}$ are

$$\bar{f}(r, \nu) \coloneqq \operatorname{acos}\left(r \sin^2 \nu + \cos \nu \sqrt{1 - r^2 \sin^2 \nu}\right), \qquad \underline{f}(r, \nu) \coloneqq \operatorname{acos}\left(r \sin^2 \nu - \cos \nu \sqrt{1 - r^2 \sin^2 \nu}\right). \tag{33}$$

Finally, to check the geometric constraints of the shoulder use the following expression:

$$\underline{\theta}_1 \leq \theta_{d_1} \leq \bar{\theta}_1. \tag{34}$$

Similarly, to avoid the singularity in $\dot{\theta}_2$ when $\sin \nu_F \to 0$, follow the same procedure. First, define a lower bound for $\sin \nu_F \geq \zeta_F > 0$, which yields

$$\underline{\nu}_F = \arcsin \zeta_F. \tag{35}$$

Second, pose the equations that define the bounds $\underline{\theta}_2$ and $\bar{\theta}_2$

$$\sin \underline{\nu}_F = \frac{d_{GJ} \sin \beta_a(\bar{\theta}_2)}{\ell_{FJ}(\bar{\theta}_2)}, \qquad \sin \underline{\nu}_F = \frac{d_{GH} \sin \beta_c(\underline{\theta}_2)}{\ell_{FH}(\underline{\theta}_2)}, \tag{36}$$

and solve for these bounds to arrive at the following expressions:

$$\underline{\theta}_2 \coloneqq 2\pi - \theta_{F_2} - \theta_H - \bar{f}\left(\frac{d_{FG}}{d_{GH}}, \underline{\nu}_F\right), \qquad \bar{\theta}_2 \coloneqq 2\pi - \theta_{F_2} - \theta_J - \underline{f}\left(\frac{d_{FG}}{d_{GJ}}, \underline{\nu}_F\right). \tag{37}$$

Table 3 Geometric limits for the joint angles of the LSMS-L35.

Joint	Joint ID i	$\underline{\theta}_i$ [deg]	$\bar{\theta}_i$ [deg]
Waist	0	−180.00	180.00
Shoulder	1	−145.95	67.10
Elbow	2	−156.56	177.07

Last, to check the geometric constraints of the elbow use the following equation:

$$\underline{\theta}_2 \leq \theta_{d_2} \leq \bar{\theta}_2. \tag{38}$$

Table3 shows the geometric limits for the joint angles of the LSMS-L35. For these computations angles $\underline{\theta}_0$ and $\bar{\theta}_0$ were set to a known conservative value based on the hardware, and $\underline{\nu}_A$ and $\underline{\nu}_F$ were set to 10 deg.

The following section derives the constraints that maintain tension on the cables, using the dynamics in Section IV.

C. Cable Tension Constraints

Cables cannot operate under compression. As a result, the LSMS must keep all cables under tension to maintain controllability over the shoulder and elbow angles. There are two types of loss of tension events for each cable:

i) An excessive cable reel out can lead to the forearm or the arm behaving like a pendulum with no direct control over their joint angles. In this case, the cable cannot apply any meaningful force on its link. The predominant forces are gravity, inertial and Coriolis effects. Notice in Figure 1 that as the elbow angle decreases and the forearm lowers, there is a point where the forearm hangs free due to gravity.

ii) The tip-over of the arm or the forearm can occur when their corresponding cables are reeled in excessively. Notice in Figure 1 that as the elbow angle increases, there is a point where cable B loses tension and the forearm tips over the elbow, hitting the arm. The tip-over of the forearm is a state from which the robot can recover autonomously. However, this event can damage the LSMS. The maneuver to recover from a tipped-over forearm is to slowly lower the arm until the forearm tips back over. The same tip-over behavior can occur with the shoulder. A tip-over event for the arm is not a state from which the LSMS can recover on its own.

the following subsections describe the constraints that avoid loss of tension events under static and dynamic conditions.

1. Static Cable Tension Constraints

To ensure that a particular goal position for the LSMS maintains tension on the cables, set $\dot{\boldsymbol{\theta}}_{\boldsymbol{d}} \equiv \mathbf{0}$ and $\ddot{\boldsymbol{\theta}}_{\boldsymbol{d}} \equiv \mathbf{0}$ and replace in Equation (23) to derive the following expression:

$$0 = \boldsymbol{\tau}_{\boldsymbol{g}}(\boldsymbol{\theta}_{\boldsymbol{d}}) + \boldsymbol{J}_G^{\top}(\boldsymbol{\theta}_{\boldsymbol{d}})^r \boldsymbol{w}_G + \boldsymbol{J}_K^{\top}(\boldsymbol{\theta}_{\boldsymbol{d}})^s \boldsymbol{w}_K + \boldsymbol{B}(\boldsymbol{\theta}_{\boldsymbol{d}})\boldsymbol{\tau}_{\boldsymbol{m}}, \tag{39}$$

Then, solving for the motor torques yields

$$\boldsymbol{\tau}_{\boldsymbol{m}} = -\boldsymbol{B}^{-1}(\boldsymbol{\theta}_{\boldsymbol{d}}) \left(\boldsymbol{\tau}_{\boldsymbol{g}}(\boldsymbol{\theta}_{\boldsymbol{d}}) + \boldsymbol{J}_G^{\top}(\boldsymbol{\theta}_{\boldsymbol{d}})^r \boldsymbol{w}_G + \boldsymbol{J}_K^{\top}(\boldsymbol{\theta}_{\boldsymbol{d}})^s \boldsymbol{w}_K \right). \tag{40}$$

Under ideal conditions, like a perfectly leveled LSMS, the expected value for τ_{m_0} is 0 $N \cdot m$, whereas the torques for motors A and B must remain above some positive threshold to maintain tension on the cables

$$\tau_{m_A} \geq \underline{\tau}_{m_A} > 0, \qquad \tau_{m_B} \geq \underline{\tau}_{m_B} > 0. \tag{41}$$

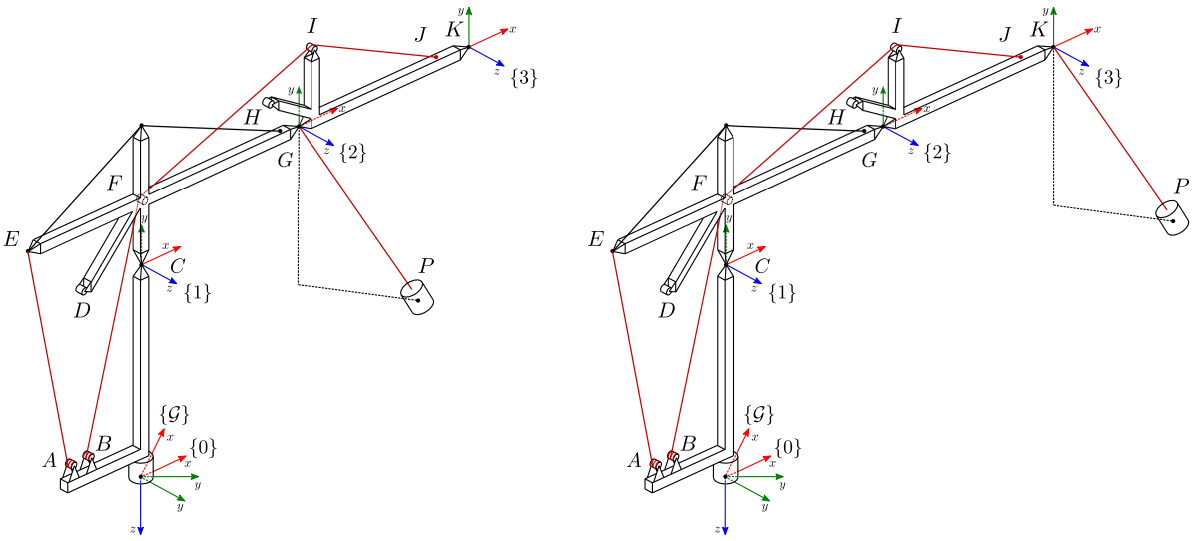
To select $\underline{\tau}_{m_A}$ and $\underline{\tau}_{m_B}$, the authors recommend a small percentage ϵ_m, for instance 10%, of the nominal motor torques required to maintain the LSMS at $\boldsymbol{\theta}_{\boldsymbol{d}} \equiv \mathbf{0}$ with no payload, that is

$$\begin{bmatrix} \underline{\tau}_{m_A} \\ \underline{\tau}_{m_B} \end{bmatrix} = -\epsilon_m \begin{bmatrix} 0 & 1 & 0 \\ 0 & 0 & 1 \end{bmatrix} \boldsymbol{B}^{-1}(\mathbf{0})\boldsymbol{\tau}_{\boldsymbol{g}}(\mathbf{0}). \tag{42}$$

Figure 9 shows the cable tension constraints given by Equations (40) and (41) for the LSMS-L35 under different loading configurations for the Earth, the Moon, and Mars. Figures 9a through 9c highlight different cable tension regions without a payload. Figures 9d through 9f depict an elbow lift with a 6-kg payload, while Figures 9g through 9i show a wrist lift with a 6-kg payload. The logistics of an elbow and wrist lift are illustrated in Figure 8.

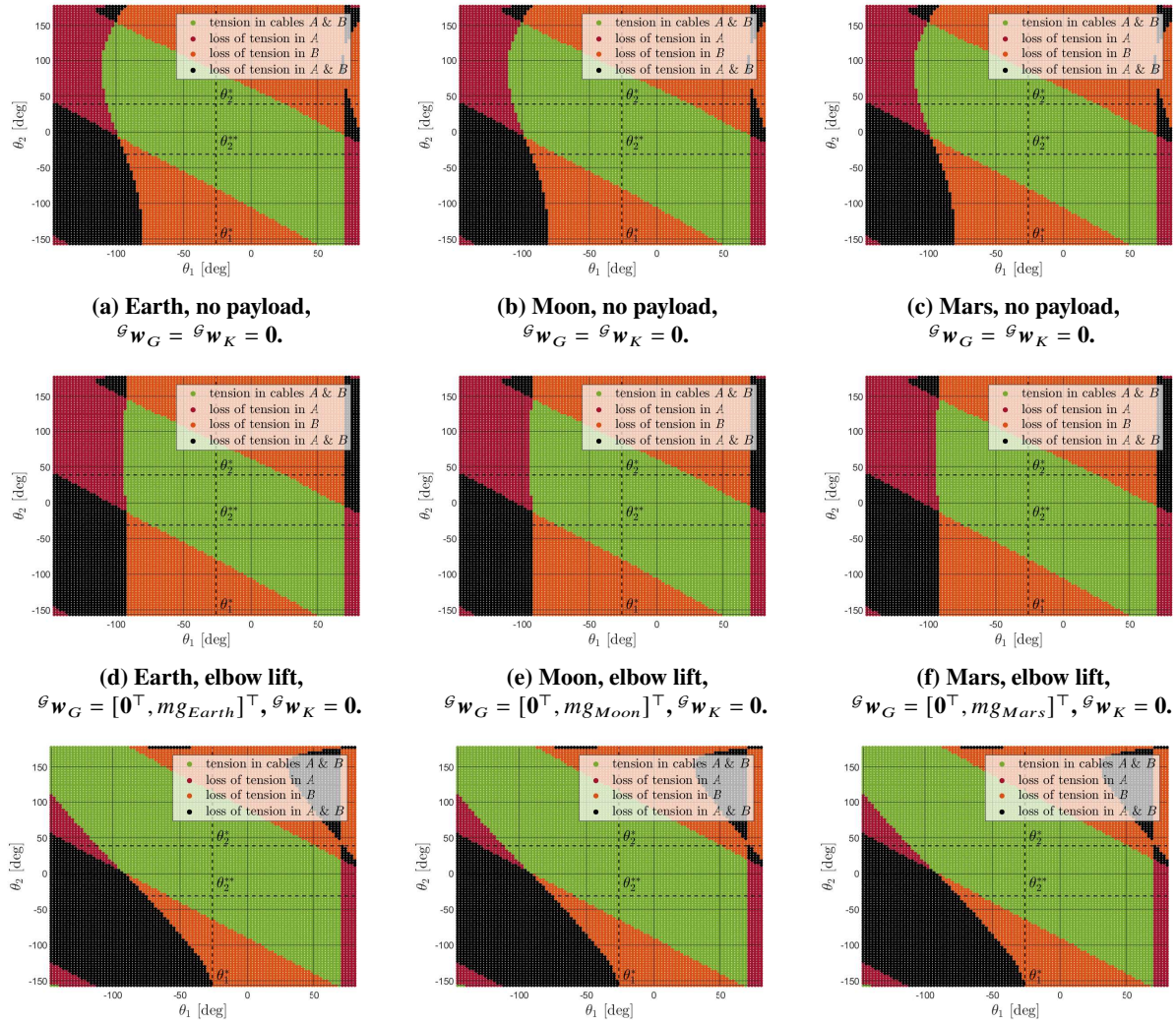
The regions of the joint space where all cables are under tension are highlighted green in Figure 9. The orange region denotes a loss of tension in cable B. The red areas mark a loss of tension in cable A, and the black regions denote a loss of tension in both cables A and B. The upper boundary of the safe region is near a forearm tip-over event, which can damage the LSMS-L35 due to its violent nature. To recover from this type of loss of tension, the shoulder must be lowered until the forearm tips over. The lower boundary of the safe region highlights a loss of tension caused when cable B is reeled out in excess. This is an easy event to recover from as long as the cable remains on the pulleys. To do so, cable B must be reeled back in. The left boundary of the safe region denotes a loss of tension on cable A caused when it is reeled out in excess. This is also an easy event to recover from. Interestingly, it is physically impossible for the LSMS-L35 to arrive at a loss of tension event through the right boundary of the safe region. This occurs because the right boundary occurs when points A, E, and C in Figure 3a align. This occurs at $\theta_1 = \theta_1^{**}$. At this point, cable A cannot pull any further, and driving θ_1 greater than θ_1^{**} would require compression on cable A.

Note that the terms on the left and right hand sides of Equation (41) scale equally with gravity. For this reason, the highlighted areas are identical across the different planetary surfaces for each type of payload lift. Next, compare the effects of the different types of payload lifts. The wrench caused by the elbow lift in Figures 9d through 9f reduces the curve on the left boundary of the safe region, pushing it closer to $\theta_1 = -90$ deg, when compared to the case with no payload. Due to the location of the center of mass of the arm and the forearm, the shoulder can go slightly below $\theta_1 = -90$ deg without losing tension on cable A. However, when the payload applies a vertical load on the elbow it pushes the shoulder closer to $\theta_1 = -90$ deg relieving the tension on the cable. On the contrary, when a payload is suspended from the wrist, the left boundary of the safe region is moved further to the left, as it adds tension to cable A, see Figures 9g through 9i. In addition, the upper and lower boundaries of the safe region shift upwards as the payload on the wrist releases tension on cable A at lower values of θ_2 and adds tension at higher values of θ_2. As expected, an elbow lift does not alter the upper and lower boundaries of the safe region, since it has no effect on the tension of cable B. Finally, the right boundary of the safe region remains unchanged across all lift configurations, as expected. The following section addresses the cable tension constraints under dynamic conditions, when the LSMS joints are subject to angular speeds and accelerations.



(a) Elbow lift. **(b) Wrist lift.**

Fig. 8 Loading configurations for the LSMS.



(a) Earth, no payload, ${}^{\mathcal{G}}\boldsymbol{w}_G = {}^{\mathcal{G}}\boldsymbol{w}_K = \mathbf{0}$.

(b) Moon, no payload, ${}^{\mathcal{G}}\boldsymbol{w}_G = {}^{\mathcal{G}}\boldsymbol{w}_K = \mathbf{0}$.

(c) Mars, no payload, ${}^{\mathcal{G}}\boldsymbol{w}_G = {}^{\mathcal{G}}\boldsymbol{w}_K = \mathbf{0}$.

(d) Earth, elbow lift, ${}^{\mathcal{G}}\boldsymbol{w}_G = [\mathbf{0}^\top, mg_{Earth}]^\top$, ${}^{\mathcal{G}}\boldsymbol{w}_K = \mathbf{0}$.

(e) Moon, elbow lift, ${}^{\mathcal{G}}\boldsymbol{w}_G = [\mathbf{0}^\top, mg_{Moon}]^\top$, ${}^{\mathcal{G}}\boldsymbol{w}_K = \mathbf{0}$.

(f) Mars, elbow lift, ${}^{\mathcal{G}}\boldsymbol{w}_G = [\mathbf{0}^\top, mg_{Mars}]^\top$, ${}^{\mathcal{G}}\boldsymbol{w}_K = \mathbf{0}$.

(g) Earth, wrist lift, ${}^{\mathcal{G}}\boldsymbol{w}_G = \mathbf{0}$, ${}^{\mathcal{G}}\boldsymbol{w}_K = [\mathbf{0}^\top, mg_{Earth}]^\top$.

(h) Moon, wrist lift, ${}^{\mathcal{G}}\boldsymbol{w}_G = \mathbf{0}$, ${}^{\mathcal{G}}\boldsymbol{w}_K = [\mathbf{0}^\top, mg_{Moon}]^\top$.

(i) Mars, wrist lift, ${}^{\mathcal{G}}\boldsymbol{w}_G = \mathbf{0}$, ${}^{\mathcal{G}}\boldsymbol{w}_K = [\mathbf{0}^\top, mg_{Mars}]^\top$.

Fig. 9 Cable tension constraints for the LSMS-L35 under static conditions, $\dot{\theta}_i \equiv \ddot{\theta}_i \equiv 0$ for all $i \in \{0, 1, 2\}$, with no payload, a payload lift from the elbow, and a payload lift from the wrist with a payload mass m of 6.00 kg. The gravitational accelerations on surface of the Earth, the Moon, and Mars are: $g_{Earth} = 9.81$ m/s^2, $g_{Moon} = 1.63$ m/s^2, and $g_{Mars} = 3.78$ m/s^2. The vectors of zeros, denoted as $\mathbf{0}$, in the wrenches above are of a appropriate size, 5 or 6 depending on the case.

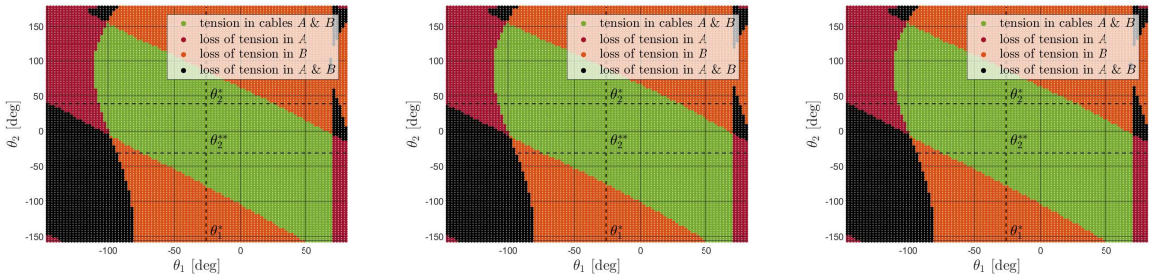
2. Dynamic Cable Tension Constraints

Repeating the same process as in Section V.C.1, with $\dot{\boldsymbol{\theta}}_{\boldsymbol{d}} \not\equiv \mathbf{0}$ and $\ddot{\boldsymbol{\theta}}_{\boldsymbol{d}} \not\equiv \mathbf{0}$, yields the dynamic constraints. This type of constraint must be checked throughout the entire trajectory, and not just at the goal position. The solution for the motor torques under dynamic conditions is given in Equation (27).

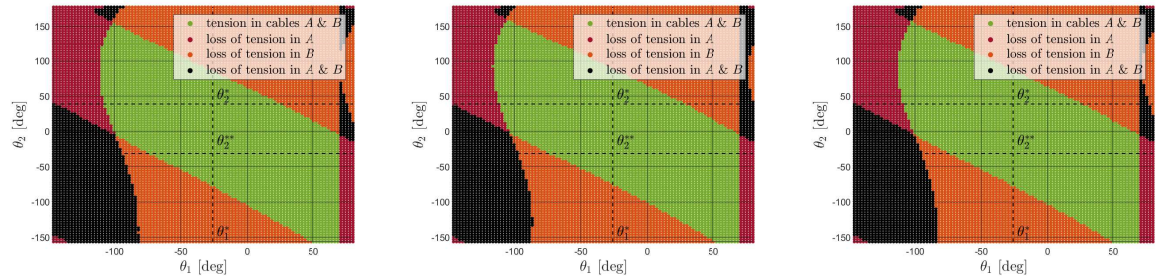
Figure 10 depicts the cable tension constraints given by Equations (27) and (41) for the LSMS-L35 under different dynamic maneuvers with no payload on different planetary surfaces. This figure evaluates the changes in the cable tension regions for rotations around different joints with a fixed angular speed, highlighting the effects of the Coriolis and centrifugal forces. The angular speeds used here are much higher than those used during operation to intensify their effect on the shape of the different regions and ease their interpretation. Figures 10a through 10c depict the effect of a rotation around the waist with a positive angular speed. The plots for a negative angular speed are not provided for brevity, since the effect is identical. Figures 10d through 10f showcase the results of a rotation around the shoulder with positive angular speed, which raises the arm; while Figures 10g through 10i present the results for a negative angular speed, which lowers the arm. Figures 10j through 10l display the effect of a rotation around the elbow with a positive angular speed, which raises the forearm; while Figures 10m through 10o highlight the results of a negative angular speed, which lowers the forearm.

Figures 10a through 10c show a small shift upward of the upper and lower boundaries of the safe region when compared to Figures 9a through 9c. As expected, the centrifugal forces relieve some tension on cable B for lower values of θ_2 and increase the tension on cable B for higher values of θ_2. Figures 10a through 10c also depict a small shift to the left of the left boundary of the safe region, since the centrifugal forces for a rotation around the waist add some tension to cable A. The predominant effect shown in Figures 10d through 10f is a shift towards the left of the left boundary of the safe region when compared to Figures 9a through 9c. This is expected since the centrifugal forces for a rotation around the shoulder with a positive angular speed add tension to cable A. So does the friction torques that occur at the shoulder. Figures 10g through 10i illustrate the opposite behavior, showing the left boundary shift towards the right, noting that a negative angular speed requires less tension on cable A. The predominant effect shown in Figures 10j through 10l is a shift upward on the upper boundary of the safe region, and a shift downward of the lower boundary. Since the tension on cable B is also propagated through the arm at point F, see Figure 1, some changes can also be observed on the left boundary of the safe region. Figures 10m through 10o show the opposite behavior, indicating that lowering the forearm at constant angular speed releases tension on cable B. As a result, the upper boundary shifts downward, and the lower boundary shifts upward. This effect reduces the size of the safe region significantly, particularly for the Moon. Notice now that the effects are not the same across the different planetary surfaces because the effects of the centrifugal forces do not scale with gravity. In fact, the effects are more noticeable on the Moon, where the gravitational forces are smaller.

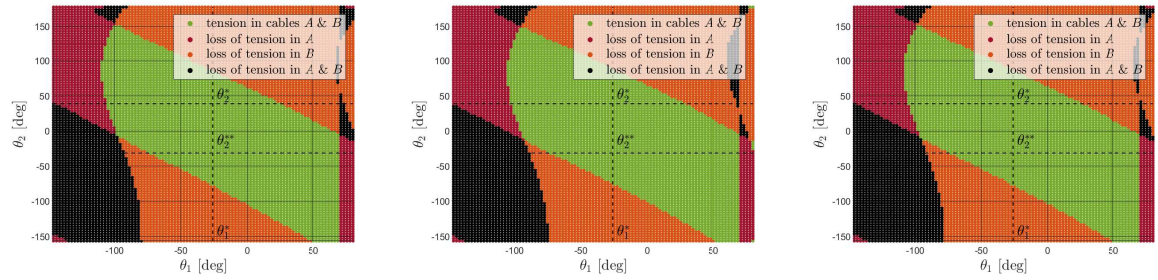
Finally, Figure 11 presents the cable tension regions for the LSMS-L35 under different maneuvers with a constant angular acceleration and zero angular speed about each of the joints. Figures 11a through 11c show little differences with respect to Figures 9a through 9c. Figures 11d through 11f show a more noticeable change when compared to Figures 9a through 9c. The left boundary of the safe region shifts towards the left, while the upper boundary moves upwards, and the lower boundary moves downward. This shift in the safe region indicates that tension is increased in all cables when the shoulder is accelerated upwards. Figures 11g through 11i exhibit the opposite behavior, indicating that cable tension is reduced when the arm and forearm are accelerated downwards. The predominant effect shown in Figures 11j through 11l is a shift upward of the upper boundary of the safe region, and a shift downward of the lower boundary, as the elbow is accelerated upwards. This trend is expected since this maneuver would increase the tension on cable B when compared to Figures 9a through 9c. Since the forces on cable B are propagated through the arm at point F, see Figure 1, this also causes some differences on the left boundary of the safe region. As expected, Figures 11m through 11o highlight the opposite behavior when the forearm is accelerated downwards, which leads to a significant decrease in the size of the safe region. Again, the shifts of the safe region are not the same across the different planetary surfaces, since the inertial effects do not scale with gravity. In fact, they are more pronounced on the Moon, where the gravitational forces are smaller.



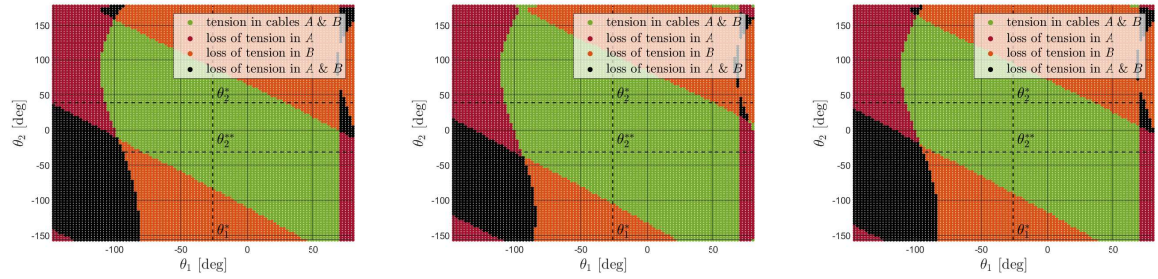
(a) Earth, $\dot{\theta}_0 = 20$ deg/s. **(b) Moon, $\dot{\theta}_0 = 20$ deg/s.** **(c) Mars, $\dot{\theta}_0 = 20$ deg/s.**



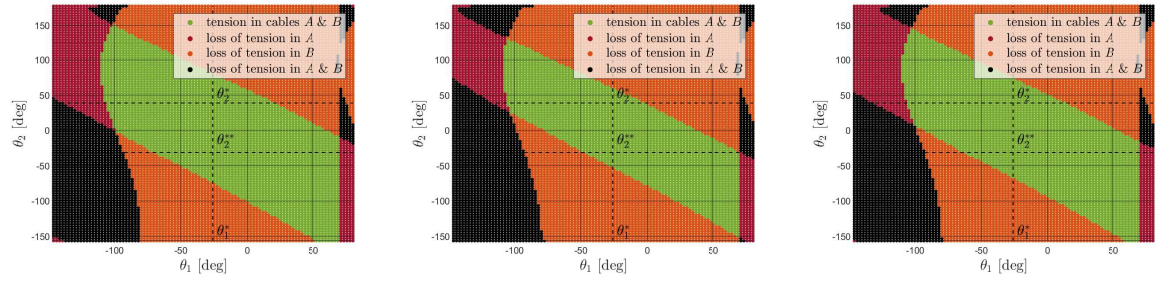
(d) Earth, $\dot{\theta}_1 = 20$ deg/s. **(e) Moon, $\dot{\theta}_1 = 20$ deg/s.** **(f) Mars, $\dot{\theta}_1 = 20$ deg/s.**



(g) Earth, $\dot{\theta}_1 = -20$ deg/s. **(h) Moon, $\dot{\theta}_1 = -20$ deg/s.** **(i) Mars, $\dot{\theta}_1 = -20$ deg/s.**

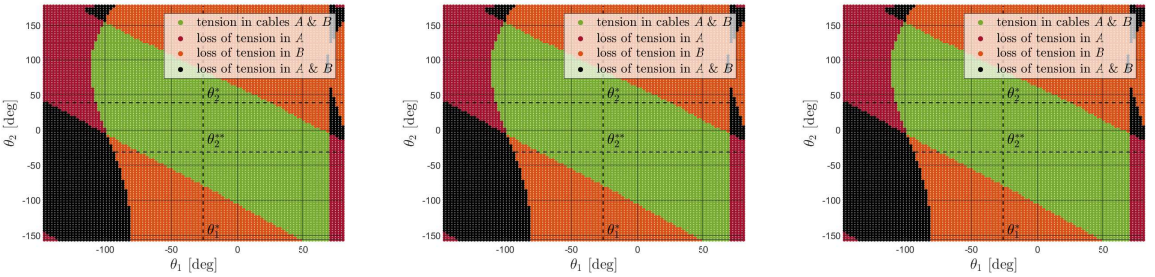


(j) Earth, $\dot{\theta}_2 = 20$ deg/s. **(k) Moon, $\dot{\theta}_2 = 20$ deg/s.** **(l) Mars, $\dot{\theta}_2 = 20$ deg/s.**

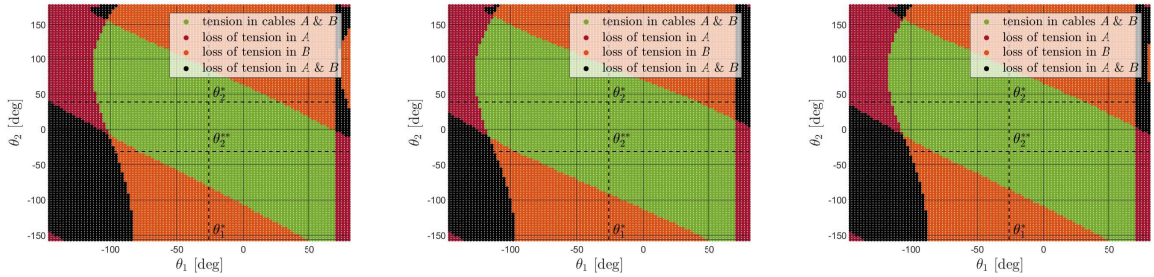


(m) Earth, $\dot{\theta}_2 = -20$ deg/s. **(n) Moon, $\dot{\theta}_2 = -20$ deg/s.** **(o) Mars, $\dot{\theta}_2 = -20$ deg/s.**

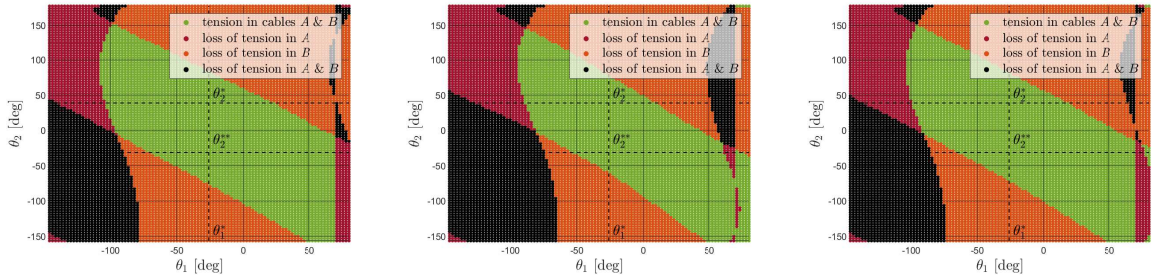
Fig. 10 Cable tension constraints under dynamic conditions, $\dot{\theta}_i \not\equiv 0$ and $\ddot{\theta}_i \equiv 0 \; \forall i \in \{0, 1, 2\}$, with no payload.



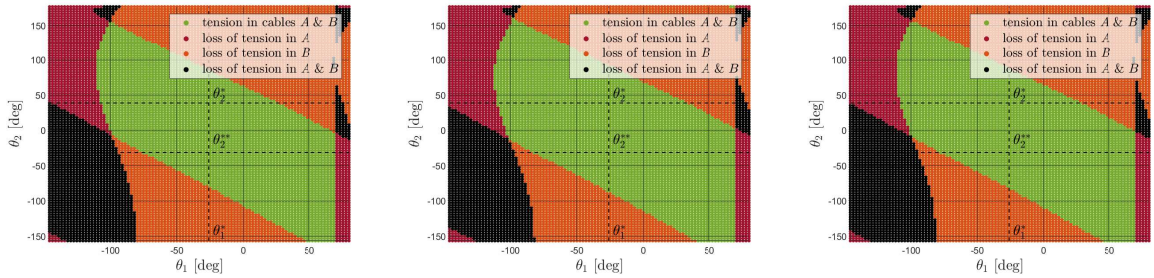
(a) Earth, $\ddot{\theta}_0 = 20$ deg/s^2. **(b) Moon, $\ddot{\theta}_0 = 20$ deg/s^2.** **(c) Mars, $\ddot{\theta}_0 = 20$ deg/s^2.**



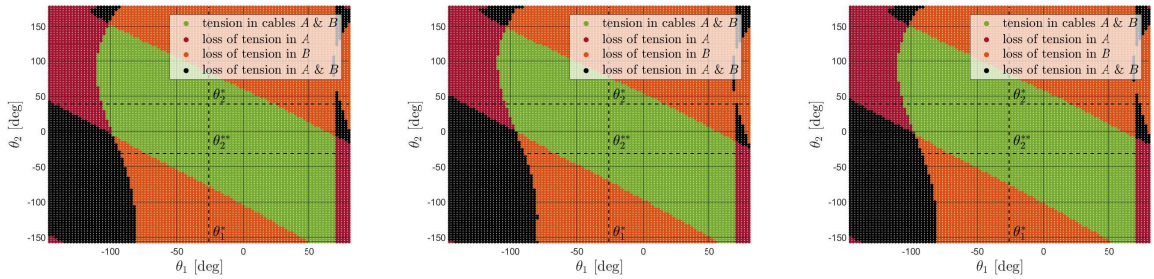
(d) Earth, $\ddot{\theta}_1 = 20$ deg/s^2. **(e) Moon, $\ddot{\theta}_1 = 20$ deg/s^2.** **(f) Mars, $\ddot{\theta}_1 = 20$ deg/s^2.**



(g) Earth, $\ddot{\theta}_1 = -20$ deg/s^2. **(h) Moon, $\ddot{\theta}_1 = -20$ deg/s^2.** **(i) Mars, $\ddot{\theta}_1 = -20$ deg/s^2.**



(j) Earth, $\ddot{\theta}_2 = 20$ deg/s^2. **(k) Moon, $\ddot{\theta}_2 = 20$ deg/s^2.** **(l) Mars, $\ddot{\theta}_2 = 20$ deg/s^2.**



(m) Earth, $\ddot{\theta}_2 = -20$ deg/s^2. **(n) Moon, $\ddot{\theta}_2 = -20$ deg/s^2.** **(o) Mars, $\ddot{\theta}_2 = -20$ deg/s^2.**

Fig. 11 Cable tension constraints under dynamic conditions, $\dot{\theta}_i \equiv 0$ and $\ddot{\theta}_i \not\equiv 0 \; \forall i \in \{0, 1, 2\}$, with no payload.

VI. Conclusion

This paper derives the safe operational envelope for the LSMS family of cable-driven cranes on different planetary bodies. To this end, this effort leverages the geometric model for the LSMS introduced in [9] and develops a new dynamic model for the LSMS. These models are used to visualize the constraints that describe the safe operational envelope for the smallest crane within the LSMS family, the LSMS-L35. The types of constraints considered are separated into three main groups: *i*) the motor constraints, characterized by the maximum motor speeds and torques; *ii*) the geometric constraints, defined by minimum and maximum waist, shoulder, and elbow angles; and *iii*) the cable tension constraints. The later are of particular importance to maintain controllability over the shoulder and elbow angles, since cables are not effective under compression loads. This paper describes two types of loss of tension events for the cables: *i*) an excessive reel out of the cables, and *ii*) a joint tip-over. The excessive reel out of a cable is an uneventful loss of tension. However, a loss of tension caused by a forearm tip-over is a relatively violent event that leads to the forearm hitting the arm. This work identifies the boundaries of the safe envelope and what kind of loss of tension events they lead to. Equations (26), (28), (29), (34), (38), and (41) fully define the safe operational envelope of the LSMS. The paper does not address self collision constraints among the different links of the LSMS, see [11] for this purpose. This work does not analyze its structural limits under different loading conditions either, see [12] for a preliminary structural analysis. Future work will leverage the safe operational envelope described here to evaluate if the trajectories generated by a kinodynamic planner are safe.

Appendix

Apply *Lagrange's equation* to the kinetic and potential energies of the LSMS, using a systematic step-by-step approach. Start with the partial derivatives of the translational and rotational kinetic energy with respect to the joint rates, and recall that ${}^{\mathcal{P}_j}\boldsymbol{I}_j$ is a constant diagonal matrix to arrive at

$$\frac{\partial T_t}{\partial \dot{\theta}_i} = \sum_{0}^{n-1}{}_j \, m_j {}^{\mathcal{G}}\boldsymbol{v}_j^{\top} \frac{\partial {}^{\mathcal{G}}\boldsymbol{v}_j}{\partial \dot{\theta}_i}, \qquad \frac{\partial T_r}{\partial \dot{\theta}_i} = \sum_{0}^{n-1}{}_j \, {}^{\mathcal{P}_j}\boldsymbol{\omega}_j^{\top {}^{\mathcal{P}_j}} \boldsymbol{I}_j \frac{\partial {}^{\mathcal{P}_j}\boldsymbol{\omega}_j}{\partial \dot{\theta}_i}. \tag{43}$$

Their derivatives with respect to time are

$$\begin{aligned} \frac{d}{dt}\left(\frac{\partial T_t}{\partial \dot{\theta}_i}\right) &= \sum_{0}^{n-1}{}_j \, m_j \left({}^{\mathcal{G}}\boldsymbol{a}_j^{\top} \frac{\partial {}^{\mathcal{G}}\boldsymbol{v}_j}{\partial \dot{\theta}_i} + {}^{\mathcal{G}}\boldsymbol{v}_j^{\top} \frac{d}{dt}\left(\frac{\partial {}^{\mathcal{G}}\boldsymbol{v}_j}{\partial \dot{\theta}_i}\right)\right), \\ \frac{d}{dt}\left(\frac{\partial T_r}{\partial \dot{\theta}_i}\right) &= \sum_{0}^{n-1}{}_j \left({}^{\mathcal{P}_j}\boldsymbol{\alpha}_j^{\top {}^{\mathcal{P}_j}} \boldsymbol{I}_j \frac{\partial {}^{\mathcal{P}_j}\boldsymbol{\omega}_j}{\partial \dot{\theta}_i} + {}^{\mathcal{P}_j}\boldsymbol{\omega}_j^{\top {}^{\mathcal{P}_j}} \boldsymbol{I}_j \frac{d}{dt}\left(\frac{\partial {}^{\mathcal{P}_j}\boldsymbol{\omega}_j}{\partial \dot{\theta}_i}\right)\right). \end{aligned} \tag{44}$$

To evaluate Equation (44), expand the partial derivatives of the linear and angular speeds of the links with respect to the joint rates using Equations (11) and (17)

$$\frac{\partial {}^{\mathcal{G}}\boldsymbol{v}_j}{\partial \dot{\theta}_i} = \begin{cases} \boldsymbol{R}_i^{\mathcal{G}} \boldsymbol{L}_z{}^i \boldsymbol{\rho}_j, & \text{if } i \le j, \\ \boldsymbol{0}, & \text{otherwise,} \end{cases} \qquad \frac{\partial {}^{\mathcal{P}_j}\boldsymbol{\omega}_j}{\partial \dot{\theta}_i} = \begin{cases} \boldsymbol{R}_j^{\mathcal{P}_j} \boldsymbol{R}_j^{i\top} \boldsymbol{e}_z, & \text{if } i \le j, \\ \boldsymbol{0}, & \text{otherwise.} \end{cases} \tag{45}$$

The time derivatives of these expressions can be further simplified using the following properties:

$$\frac{d\boldsymbol{R}_i^{\mathcal{G}}}{dt} = \sum_{0}^{i}{}_k \, \dot{\theta}_k \boldsymbol{R}_k^{\mathcal{G}} \boldsymbol{L}_z \boldsymbol{R}_i^k, \qquad \frac{d{}^i\boldsymbol{\rho}_j}{dt} = \sum_{i+1}^{j}{}_k \, \dot{\theta}_k \boldsymbol{R}_k^i \boldsymbol{L}_z{}^k \boldsymbol{\rho}_j, \qquad \frac{d\boldsymbol{R}_j^{\mathcal{P}_j}}{dt} = 0, \qquad \frac{d\boldsymbol{R}_j^i}{dt} = \sum_{i+1}^{j}{}_k \, \dot{\theta}_k \boldsymbol{R}_k^i \boldsymbol{L}_z \boldsymbol{R}_j^k, \tag{46}$$

for all $i \le j$, yielding the following results:

$$\frac{d}{dt}\left(\frac{\partial {}^{\mathcal{G}}\boldsymbol{v}_j}{\partial \dot{\theta}_i}\right) = \begin{cases} \sum_{0}^{i}{}_k \, \dot{\theta}_k \boldsymbol{R}_k^{\mathcal{G}} \boldsymbol{L}_z \boldsymbol{R}_i^k \boldsymbol{L}_z{}^i \boldsymbol{\rho}_j + \sum_{i+1}^{j}{}_k \, \dot{\theta}_k \boldsymbol{R}_i^{\mathcal{G}} \boldsymbol{L}_z \boldsymbol{R}_k^i \boldsymbol{L}_z{}^k \boldsymbol{\rho}_j, & \text{if } i \le j, \\ \boldsymbol{0}, & \text{otherwise.} \end{cases} \tag{47}$$

$$\frac{d}{dt}\left(\frac{\partial {}^{\mathcal{P}_j}\boldsymbol{\omega}_j}{\partial \dot{\theta}_i}\right) = \begin{cases} \boldsymbol{R}_j^{\mathcal{P}_j} \sum_{i+1}^{j}{}_k \, \dot{\theta}_k \boldsymbol{R}_j^{k\top} \boldsymbol{L}_z^{\top} \boldsymbol{R}_k^{i\top} \boldsymbol{e}_z, & \text{if } i \le j, \\ \boldsymbol{0}, & \text{otherwise.} \end{cases} \tag{48}$$

Combining these expressions with Equations (11), (15), (17), and (19) yields

$$
\begin{aligned}
{}^{\mathcal{G}}\boldsymbol{a}_j^{\top}\frac{\partial {}^{\mathcal{G}}\boldsymbol{v}_j}{\partial \dot{\theta}_i} = {} & \sum_{0}^{j}{}_k \ddot{\theta}_k{}^k \boldsymbol{\rho}_j^{\top}\boldsymbol{L}_z^{\top}\boldsymbol{R}_i^k\boldsymbol{L}_z{}^i\boldsymbol{\rho}_j + \\
& \sum_{0}^{j}{}_k \sum_{0}^{k}{}_\ell \dot{\theta}_k\dot{\theta}_\ell{}^k \boldsymbol{\rho}_j^{\top}\boldsymbol{L}_z^{\top}\boldsymbol{R}_k^{\ell\top}\boldsymbol{L}_z^{\top}\boldsymbol{R}_i^\ell\boldsymbol{L}_z{}^i\boldsymbol{\rho}_j + \sum_{0}^{j}{}_k \sum_{k+1}^{j}{}_\ell \dot{\theta}_k\dot{\theta}_\ell{}^\ell \boldsymbol{\rho}_j^{\top}\boldsymbol{L}_z^{\top}\boldsymbol{R}_\ell^{k\top}\boldsymbol{L}_z^{\top}\boldsymbol{R}_i^k\boldsymbol{L}_z{}^i\boldsymbol{\rho}_j, \qquad (49)
\end{aligned}
$$

$$
{}^{\mathcal{G}}\boldsymbol{v}_j^{\top}\frac{d}{dt}\left(\frac{\partial {}^{\mathcal{G}}\boldsymbol{v}_j}{\partial \dot{\theta}_i}\right) = \sum_{0}^{j}{}_k \sum_{0}^{i}{}_\ell \dot{\theta}_k\dot{\theta}_\ell{}^k \boldsymbol{\rho}_j^{\top}\boldsymbol{L}_z^{\top}\boldsymbol{R}_\ell^k\boldsymbol{L}_z\boldsymbol{R}_i^\ell\boldsymbol{L}_z{}^i\boldsymbol{\rho}_j + \sum_{0}^{j}{}_k \sum_{i+1}^{j}{}_\ell \dot{\theta}_k\dot{\theta}_\ell{}^k \boldsymbol{\rho}_j^{\top}\boldsymbol{L}_z^{\top}\boldsymbol{R}_i^k\boldsymbol{L}_z\boldsymbol{R}_\ell^i\boldsymbol{L}_z{}^\ell\boldsymbol{\rho}_j, \qquad (50)
$$

$$
{}^{\mathcal{P}_j}\boldsymbol{\alpha}_j^{\top\mathcal{P}_j}\boldsymbol{I}_j\frac{\partial {}^{\mathcal{P}_j}\boldsymbol{\omega}_j}{\partial \dot{\theta}_i} = \sum_{0}^{j}{}_k \ddot{\theta}_k\boldsymbol{e}_z^{\top}\boldsymbol{R}_j^{k\,j}\boldsymbol{I}_j\boldsymbol{R}_j^{i\,\top}\boldsymbol{e}_z + \sum_{0}^{j}{}_k \sum_{k+1}^{j}{}_\ell \dot{\theta}_k\dot{\theta}_\ell\boldsymbol{e}_z^{\top}\boldsymbol{R}_\ell^k\boldsymbol{L}_z\boldsymbol{R}_j^{\ell\,j}\boldsymbol{I}_j\boldsymbol{R}_j^{i\,\top}\boldsymbol{e}_z, \qquad (51)
$$

$$
{}^{\mathcal{P}_j}\boldsymbol{\omega}_j^{\top\mathcal{P}_j}\boldsymbol{I}_j\frac{d}{dt}\left(\frac{\partial {}^{\mathcal{P}_j}\boldsymbol{\omega}_j}{\partial \dot{\theta}_i}\right) = \sum_{0}^{j}{}_k \sum_{i+1}^{j}{}_\ell \dot{\theta}_k\dot{\theta}_\ell\boldsymbol{e}_z^{\top}\boldsymbol{R}_j^{k\,j}\boldsymbol{I}_j\boldsymbol{R}_j^{\ell\,\top}\boldsymbol{L}_z^{\top}\boldsymbol{R}_\ell^{i\,\top}\boldsymbol{e}_z, \qquad (52)
$$

for all $i \leq j$, otherwise all the terms above are 0, and with ${}^j\boldsymbol{I}_j \coloneqq \boldsymbol{R}_j^{\mathcal{P}_j\top\mathcal{P}_j}\boldsymbol{I}_j\boldsymbol{R}_j^{\mathcal{P}_j}$ being the inertia matrix of the jth joint rotated to match the directions of reference frame $\{j\}$. Recall these expressions are necessary to evaluate Equation (44).

Next, the partial derivatives of the translational and rotational kinetic energies with respect to the joint angles are

$$
\frac{\partial T_t}{\partial \theta_i} = \sum_{0}^{n-1}{}_j m_j{}^{\mathcal{G}}\boldsymbol{v}_j^{\top}\frac{\partial {}^{\mathcal{G}}\boldsymbol{v}_j}{\partial \theta_i}, \qquad \frac{\partial T_r}{\partial \theta_i} = \sum_{0}^{n-1}{}_j {}^{\mathcal{P}_j}\boldsymbol{\omega}_j^{\top\mathcal{P}_j}\boldsymbol{I}_j\frac{\partial {}^{\mathcal{P}_j}\boldsymbol{\omega}_j}{\partial \theta_i}. \qquad (53)
$$

To evaluate Equation (53), expand the partial derivatives of the linear and angular speeds of the links with respect to the joint angles using Equations (11) and (17), and use properties

$$
\frac{\partial \boldsymbol{R}_k^{\mathcal{G}}}{\partial \theta_i} = \begin{cases} \boldsymbol{R}_i^{\mathcal{G}}\boldsymbol{L}_z\boldsymbol{R}_k^i, & \text{if } i \leq k, \\ \boldsymbol{0}, & \text{otherwise,} \end{cases} \quad \frac{\partial {}^k\boldsymbol{\rho}_j}{\partial \theta_i} = \begin{cases} \boldsymbol{R}_i^k\boldsymbol{L}_z{}^i\boldsymbol{\rho}_j, & \text{if } k < i \leq j, \\ \boldsymbol{0}, & \text{otherwise,} \end{cases} \quad \frac{\partial \boldsymbol{R}_j^k}{\partial \theta_i} = \begin{cases} \boldsymbol{R}_i^k\boldsymbol{L}_z\boldsymbol{R}_j^i, & \text{if } k < i \leq j, \\ \boldsymbol{0}, & \text{otherwise,} \end{cases} \qquad (54)
$$

to arrive at the following result:

$$
\frac{\partial {}^{\mathcal{G}}\boldsymbol{v}_j}{\partial \theta_i} = \begin{cases} \sum_{0}^{i-1}{}_k \dot{\theta}_k\boldsymbol{R}_k^{\mathcal{G}}\boldsymbol{L}_z\boldsymbol{R}_i^k\boldsymbol{L}_z{}^i\boldsymbol{\rho}_j + \sum_{i}^{j}{}_k \dot{\theta}_k\boldsymbol{R}_i^{\mathcal{G}}\boldsymbol{L}_z\boldsymbol{R}_k^i\boldsymbol{L}_z{}^k\boldsymbol{\rho}_j, & \text{if } i \leq j, \\ \boldsymbol{0}, & \text{otherwise,} \end{cases} \qquad (55)
$$

$$
\frac{\partial {}^{\mathcal{P}_j}\boldsymbol{\omega}_j}{\partial \theta_i} = \begin{cases} \boldsymbol{R}_j^{\mathcal{P}_j}\sum_{0}^{i-1}{}_k \dot{\theta}_k\boldsymbol{R}_j^{i\,\top}\boldsymbol{L}_z^{\top}\boldsymbol{R}_i^{k\,\top}\boldsymbol{e}_z, & \text{if } i \leq j, \\ \boldsymbol{0}, & \text{otherwise.} \end{cases} \qquad (56)
$$

Combining these with Equations (11) and (17) yields

$$
{}^{\mathcal{G}}\boldsymbol{v}_j^{\top}\frac{\partial {}^{\mathcal{G}}\boldsymbol{v}_j}{\partial \theta_i} = \sum_{0}^{j}{}_k \sum_{0}^{i-1}{}_\ell \dot{\theta}_k\dot{\theta}_\ell{}^k \boldsymbol{\rho}_j^{\top}\boldsymbol{L}_z^{\top}\boldsymbol{R}_\ell^k\boldsymbol{L}_z\boldsymbol{R}_i^\ell\boldsymbol{L}_z{}^i\boldsymbol{\rho}_j + \sum_{0}^{j}{}_k \sum_{i}^{j}{}_\ell \dot{\theta}_k\dot{\theta}_\ell{}^k \boldsymbol{\rho}_j^{\top}\boldsymbol{L}_z^{\top}\boldsymbol{R}_i^k\boldsymbol{L}_z\boldsymbol{R}_\ell^i\boldsymbol{L}_z{}^\ell\boldsymbol{\rho}_j, \qquad (57)
$$

$$
{}^{\mathcal{P}_j}\boldsymbol{\omega}_j^{\top\mathcal{P}_j}\boldsymbol{I}_j\frac{\partial {}^{\mathcal{P}_j}\boldsymbol{\omega}_j}{\partial \theta_i} = \sum_{0}^{j}{}_k \sum_{0}^{i-1}{}_\ell \dot{\theta}_k\dot{\theta}_\ell\boldsymbol{e}_z^{\top}\boldsymbol{R}_j^{k\,j}\boldsymbol{I}_j\boldsymbol{R}_j^{i\,\top}\boldsymbol{L}_z^{\top}\boldsymbol{R}_i^{\ell\,\top}\boldsymbol{e}_z, \qquad (58)
$$

for all $i \leq j$, otherwise all the terms above are 0. Recall these expressions are necessary to evaluate Equation (53). Now, grouping the terms arising from the translational and rotational kinetic energies, combined with a simple manipulation the summation limits, and noting that

$$
{}^{\mathcal{G}}\boldsymbol{v}_j^{\top}\frac{d}{dt}\left(\frac{\partial {}^{\mathcal{G}}\boldsymbol{v}_j}{\partial \dot{\theta}_i}\right) - {}^{\mathcal{G}}\boldsymbol{v}_j^{\top}\frac{\partial {}^{\mathcal{G}}\boldsymbol{v}_j}{\partial \theta_i} = 0, \qquad (59)
$$

leads to the following results:

$$\frac{d}{dt}\left(\frac{\partial T_t}{\partial \dot{\theta}_i}\right) - \frac{\partial T_t}{\partial \theta_i} = \sum_{i}^{n-1}{}_j\, m_j \sum_{0}^{j}{}_k \left(\ddot{\theta}_k{}^k \boldsymbol{\rho}_j^\top \boldsymbol{L}_z^\top \boldsymbol{R}_i^k \boldsymbol{L}_z{}^i \boldsymbol{\rho}_j + \sum_{0}^{k}{}_\ell\, \dot{\theta}_k \dot{\theta}_\ell{}^k \boldsymbol{\rho}_j^\top \boldsymbol{L}_z^\top \boldsymbol{R}_k^{\ell\top} \boldsymbol{L}_z^\top \boldsymbol{R}_i^\ell \boldsymbol{L}_z{}^i \boldsymbol{\rho}_j + \right.$$
$$\left. \sum_{k+1}^{j}{}_\ell\, \dot{\theta}_k \dot{\theta}_\ell{}^\ell \boldsymbol{\rho}_j^\top \boldsymbol{L}_z^\top \boldsymbol{R}_\ell^{k\top} \boldsymbol{L}_z^\top \boldsymbol{R}_i^k \boldsymbol{L}_z{}^i \boldsymbol{\rho}_j \right), \tag{60}$$

$$\frac{d}{dt}\left(\frac{\partial T_r}{\partial \dot{\theta}_i}\right) - \frac{\partial T_r}{\partial \theta_i} = \sum_{i}^{n-1}{}_j \sum_{0}^{j}{}_k \left(\ddot{\theta}_k \boldsymbol{e}_z^\top \boldsymbol{R}_j^{kj} \boldsymbol{I}_j \boldsymbol{R}_j^{i\top} \boldsymbol{e}_z + \sum_{k+1}^{j}{}_\ell\, \dot{\theta}_k \dot{\theta}_\ell \boldsymbol{e}_z^\top \boldsymbol{R}_\ell^k \boldsymbol{L}_z \boldsymbol{R}_j^{\ell j} \boldsymbol{I}_j \boldsymbol{R}_j^{i\top} \boldsymbol{e}_z + \right.$$
$$\left. \sum_{i+1}^{j}{}_\ell\, \dot{\theta}_k \dot{\theta}_\ell \boldsymbol{e}_z^\top \boldsymbol{R}_\ell^i \boldsymbol{L}_z \boldsymbol{R}_j^{\ell j} \boldsymbol{I}_j \boldsymbol{R}_j^{k\top} \boldsymbol{e}_z - \sum_{0}^{i-1}{}_\ell\, \dot{\theta}_k \dot{\theta}_\ell \boldsymbol{e}_z^\top \boldsymbol{R}_i^\ell \boldsymbol{L}_z \boldsymbol{R}_j^{ij} \boldsymbol{I}_j \boldsymbol{R}_j^{k\top} \boldsymbol{e}_z \right). \tag{61}$$

for all $i \leq j$, otherwise all the terms above are 0. Then, one can extract elements (p, q) of the generalized inertia and Coriolis matrices from the expressions above by setting $i = p$, $k = q$, and noting that $\ddot{\theta}_q$ will not appear in the expressions unless $j \geq q$. Thus, the coefficient for the second time derivative of the qth joint angle, located in the pth row of the generalized inertia matrix is

$$I_{pq} = \sum_{\max(p,q)}^{n-1}{}_j \left(m_j{}^q \boldsymbol{\rho}_j^\top \boldsymbol{L}_z^\top \boldsymbol{R}_p^q \boldsymbol{L}_z{}^p \boldsymbol{\rho}_j + \boldsymbol{e}_z^\top \boldsymbol{R}_j^{qj} \boldsymbol{I}_j \boldsymbol{R}_j^{p\top} \boldsymbol{e}_z \right), \qquad \forall p, q \in \{0, \ldots, n-1\}. \tag{62}$$

Notice that the matrix is symmetric, as expected, and for $p = q$ the elements of the generalized inertia matrix can be further simplified to

$$I_{pp} = \sum_{p}^{n-1}{}_j \left(m_j{}^p \boldsymbol{\rho}_j^\top \boldsymbol{L}_z^\top \boldsymbol{L}_z{}^p \boldsymbol{\rho}_j + \boldsymbol{e}_z^\top \boldsymbol{R}_j^{pj} \boldsymbol{I}_j \boldsymbol{R}_j^{p\top} \boldsymbol{e}_z \right), \qquad \forall p \in \{0, \ldots, n-1\}. \tag{63}$$

Similarly, one can extract elements (p, q) of the generalized matrix responsible for the Coriolis and centrifugal forces. Thus, the coefficient for the first time derivative of the qth joint angle, located in the pth row of the generalized Coriolis and centrifugal forces matrix is

$$C_{pq} = \sum_{\max(p,q)}^{n-1}{}_j \left(m_j \sum_{0}^{q}{}_\ell\, \dot{\theta}_\ell{}^q \boldsymbol{\rho}_j^\top \boldsymbol{L}_z^\top \boldsymbol{R}_q^{\ell\top} \boldsymbol{L}_z^\top \boldsymbol{R}_p^\ell \boldsymbol{L}_z{}^p \boldsymbol{\rho}_j + m_j \sum_{q+1}^{j}{}_\ell\, \dot{\theta}_\ell{}^\ell \boldsymbol{\rho}_j^\top \boldsymbol{L}_z^\top \boldsymbol{R}_\ell^{q\top} \boldsymbol{L}_z^\top \boldsymbol{R}_p^q \boldsymbol{L}_z{}^p \boldsymbol{\rho}_j + \right.$$
$$\left. \sum_{p+1}^{j}{}_\ell\, \dot{\theta}_\ell \boldsymbol{e}_z^\top \boldsymbol{R}_\ell^p \boldsymbol{L}_z \boldsymbol{R}_j^{\ell j} \boldsymbol{I}_j \boldsymbol{R}_j^{q\top} \boldsymbol{e}_z + \sum_{q+1}^{j}{}_\ell\, \dot{\theta}_\ell \boldsymbol{e}_z^\top \boldsymbol{R}_\ell^q \boldsymbol{L}_z \boldsymbol{R}_j^{\ell j} \boldsymbol{I}_j \boldsymbol{R}_j^{p\top} \boldsymbol{e}_z - \sum_{0}^{p-1}{}_\ell\, \dot{\theta}_\ell \boldsymbol{e}_z^\top \boldsymbol{R}_p^\ell \boldsymbol{L}_z \boldsymbol{R}_j^{pj} \boldsymbol{I}_j \boldsymbol{R}_j^{q\top} \boldsymbol{e}_z \right), \tag{64}$$

for all $p, q \in \{0, \ldots, n-1\}$. When $p = q$ this expression can be further simplified, noting that for any vector $\boldsymbol{v} \in \mathbb{R}^3$ the following property holds $\boldsymbol{v}^\top \boldsymbol{L}_z \boldsymbol{v} = 0$, which yields

$$C_{pp} = \sum_{p}^{n-1}{}_j \left(\sum_{p+1}^{j}{}_\ell\, \dot{\theta}_\ell \left(m_j{}^\ell \boldsymbol{\rho}_j^\top \boldsymbol{L}_z^\top \boldsymbol{R}_\ell^{p\top} \boldsymbol{L}_z^\top \boldsymbol{L}_z{}^p \boldsymbol{\rho}_j + 2 \boldsymbol{e}_z^\top \boldsymbol{R}_\ell^p \boldsymbol{L}_z \boldsymbol{R}_j^{\ell j} \boldsymbol{I}_j \boldsymbol{R}_j^{p\top} \boldsymbol{e}_z \right) - \sum_{0}^{p-1}{}_\ell\, \dot{\theta}_\ell \boldsymbol{e}_z^\top \boldsymbol{R}_p^\ell \boldsymbol{L}_z \boldsymbol{R}_j^{pj} \boldsymbol{I}_j \boldsymbol{R}_j^{p\top} \boldsymbol{e}_z \right). \tag{65}$$

Next, compute the partial derivatives of the potential energy with respect to the joint angles to find the contribution of gravity to the equations of motion. As a result, the torques at the joints due to the gravitational forces are $\boldsymbol{\tau_g} \coloneqq \left[\tau_{g_0}, \tau_{g_1}, \tau_{g_2}\right]^\top$ where

$$\tau_{g_p} \coloneqq -\frac{\partial V}{\partial \theta_p} = g \boldsymbol{e}_z^\top \boldsymbol{R}_p^{\mathcal{G}} \boldsymbol{L}_z \sum_{p}^{n-1}{}_j\, m_j{}^p \boldsymbol{\rho}_j. \tag{66}$$

Dry friction is used to model the dissipation forces acting on the LSMS. As a result, the joint torques due to friction are $\boldsymbol{\tau_d} \coloneqq \left[\tau_{d_0}, \tau_{d_1}, \tau_{d_2}\right]^\top$ with

$$\tau_{d_p} = -\tau_{D_p} \tanh\left(\frac{\dot{\theta}_p}{\dot{\theta}_{D_p}}\right), \tag{67}$$

where $\tau_{D_p} > 0$ represents the dynamic friction torque at the pth joint when $\dot{\theta}_p \to \infty$; and $\dot{\theta}_{D_p} > 0$ captures the joint speed at which 76% of the dynamic friction torque is achieved.

Now, consider a payload suspended from the elbow, applying a torque $\boldsymbol{n}_G$ and a force $\boldsymbol{f}_G$ at point G. Assume that the corresponding wrench ${}^r\boldsymbol{w}_G \coloneqq \left[{}^r\boldsymbol{n}_G^\top, {}^r\boldsymbol{f}_G^\top\right]^\top$ is expressed in the rth frame. Then the contributions to the pth joint torque caused by the payload torques and forces are

$$\tau_{n_p} = \begin{cases} \boldsymbol{e}_z^\top \boldsymbol{R}_r^p \, {}^r\boldsymbol{n}_G, & \text{if } p \leq 1, \\ 0, & \text{otherwise,} \end{cases} \qquad \text{and} \qquad \tau_{f_p} = \begin{cases} {}^p\boldsymbol{p}_G^\top \boldsymbol{L}_z^\top \boldsymbol{R}_r^{pr} \boldsymbol{f}_G, & \text{if } p \leq 1, \\ 0, & \text{otherwise.} \end{cases} \tag{68}$$

The result above was achieved using the property of the mixed product $\boldsymbol{a} \cdot (\boldsymbol{b} \times \boldsymbol{c}) = (\boldsymbol{a} \times \boldsymbol{b}) \cdot \boldsymbol{c}$, and the matrix expression for the cross product $\boldsymbol{e}_z \times \boldsymbol{b} = \boldsymbol{L}_z \, \boldsymbol{b}$, applied to $\boldsymbol{e}_z \cdot \left({}^p\boldsymbol{p}_G \times \boldsymbol{R}_r^{pr} \boldsymbol{f}_G\right)$, which extracts the z component of the cross product between the moment arm and the force, expressed in the pth frame. Consequently, the Jacobian matrix for the elbow is

$$\boldsymbol{J}_G^\top \coloneqq \begin{bmatrix} \boldsymbol{e}_z^\top \boldsymbol{R}_r^0 & {}^0\boldsymbol{p}_G^\top \boldsymbol{L}_z^\top \boldsymbol{R}_r^0 \\ \boldsymbol{e}_z^\top \boldsymbol{R}_r^1 & {}^1\boldsymbol{p}_G^\top \boldsymbol{L}_z^\top \boldsymbol{R}_r^1 \\ \boldsymbol{0} & \boldsymbol{0} \end{bmatrix}. \tag{69}$$

Similarly, considering that the LSMS has a payload suspended from the end effector, applying a torque $\boldsymbol{n}_K$ and a force $\boldsymbol{f}_K$ at point K. Assuming the resulting wrench ${}^s\boldsymbol{w}_K \coloneqq \left[{}^s\boldsymbol{n}_K^\top, {}^s\boldsymbol{f}_K^\top\right]^\top$ is expressed in the sth frame yields the following Jacobian for the end effector:

$$\boldsymbol{J}_K^\top \coloneqq \begin{bmatrix} \boldsymbol{e}_z^\top \boldsymbol{R}_s^0 & {}^0\boldsymbol{p}_K^\top \boldsymbol{L}_z^\top \boldsymbol{R}_s^0 \\ \boldsymbol{e}_z^\top \boldsymbol{R}_s^1 & {}^1\boldsymbol{p}_K^\top \boldsymbol{L}_z^\top \boldsymbol{R}_s^1 \\ \boldsymbol{e}_z^\top \boldsymbol{R}_s^2 & {}^2\boldsymbol{p}_K^\top \boldsymbol{L}_z^\top \boldsymbol{R}_s^2 \end{bmatrix}. \tag{70}$$

Finally, to compute the control matrix $\boldsymbol{B}(\boldsymbol{\theta})$, consider the gear ratios i_0, i_A, and i_B, as well as the efficiency η_0, η_A, and η_B of the motors and gearboxes. Then, the torques at the output of the gearboxes are

$$\tau_0 = \frac{\eta_0}{i_0} \tau_{m_0}, \qquad \tau_A = \frac{\eta_A}{i_A} \tau_{m_A}, \qquad \tau_B = \frac{\eta_B}{i_B} \tau_{m_B}, \tag{71}$$

where τ_{m_0}, τ_{m_A}, and τ_{m_B} are the torques of the motors located at points 0, A, and B. Next, the magnitude of the forces that motors A and B apply onto the corresponding cables is

$$f_A = \frac{\eta_A}{i_A r_A} \tau_{m_A}, \qquad f_B = \frac{\eta_B}{i_B r_B} \tau_{m_B}. \tag{72}$$

These lead to the following forces applied onto the attachment points E and J:

$${}^1\boldsymbol{f}_E = \begin{cases} f_A \, {}^1\boldsymbol{u}_{EA}, & \text{if } \theta_1 \geq \theta_1^*, \\ f_A \, {}^1\boldsymbol{u}_{ED}, & \text{otherwise,} \end{cases} \qquad {}^2\boldsymbol{f}_J = \begin{cases} f_B \, {}^2\boldsymbol{u}_{JF}, & \text{if } \theta_2 \geq \theta_2^*, \\ f_B \, {}^2\boldsymbol{u}_{JI}, & \text{otherwise,} \end{cases} \tag{73}$$

where the unit vectors above can be computed using the following formula:

$${}^k\boldsymbol{u}_{XY} \coloneqq \frac{{}^k\boldsymbol{v}_{XY}}{\left\| {}^k\boldsymbol{v}_{XY} \right\|}, \tag{74}$$

with vectors

$$\begin{aligned} {}^1\boldsymbol{v}_{EA} &= -\left(\boldsymbol{R}_1^{0\top} {}^0\boldsymbol{v}_{AC} + {}^1\boldsymbol{v}_{CE}\right), & {}^1\boldsymbol{v}_{ED} &= {}^1\boldsymbol{v}_{CD} - {}^1\boldsymbol{v}_{CE}, \\ {}^2\boldsymbol{v}_{JF} &= -\left(\boldsymbol{R}_2^{1\top} {}^1\boldsymbol{v}_{FG} + {}^2\boldsymbol{v}_{GJ}\right), & {}^2\boldsymbol{v}_{JI} &= {}^2\boldsymbol{v}_{GI} - {}^2\boldsymbol{v}_{GJ}. \end{aligned} \tag{75}$$

The forces applied onto the spreaders D, F, I, and H can be computed as follows:

$$\begin{aligned} {}^1\boldsymbol{f}_D &= \begin{cases} \boldsymbol{0}, & \text{if } \theta_1 \geq \theta_1^*, \\ f_A \left({}^1\boldsymbol{u}_{DA} + {}^1\boldsymbol{u}_{DE}\right) & \text{otherwise,} \end{cases} \qquad {}^1\boldsymbol{f}_F = \begin{cases} f_B \left({}^1\boldsymbol{u}_{FB} + {}^1\boldsymbol{u}_{FJ}\right), & \text{if } \theta_2 \geq \theta_2^*, \\ f_B \left({}^1\boldsymbol{u}_{FB} + {}^1\boldsymbol{u}_{FI}\right), & \text{if } \theta_2^{**} \leq \theta_2 < \theta_2^*, \\ f_B \left({}^1\boldsymbol{u}_{FB} + {}^1\boldsymbol{u}_{FH}\right), & \text{if } \theta_2 < \theta_2^{**}, \end{cases} \\ {}^2\boldsymbol{f}_H &= \begin{cases} \boldsymbol{0}, & \text{if } \theta_2 \geq \theta_2^{**}, \\ f_B \left({}^2\boldsymbol{u}_{HF} + {}^2\boldsymbol{u}_{HI}\right) & \text{otherwise,} \end{cases} \qquad {}^2\boldsymbol{f}_I = \begin{cases} \boldsymbol{0}, & \text{if } \theta_2 \geq \theta_2^*, \\ f_B \left({}^2\boldsymbol{u}_{IJ} + {}^2\boldsymbol{u}_{IF}\right), & \text{if } \theta_2^{**} \leq \theta_2 < \theta_2^*, \\ f_B \left({}^2\boldsymbol{u}_{IJ} + {}^2\boldsymbol{u}_{IH}\right), & \text{if } \theta_2 < \theta_2^{**}, \end{cases} \end{aligned} \tag{76}$$

where the unit vectors ${}^1\boldsymbol{u}_{DA}$, ${}^1\boldsymbol{u}_{FB}$, ${}^1\boldsymbol{u}_{FI}$, ${}^1\boldsymbol{u}_{FH}$, ${}^1\boldsymbol{u}_{HI}$, and ${}^1\boldsymbol{u}_{IF}$ can be computed using Equation (74) with vectors

$$\begin{aligned} {}^1\boldsymbol{v}_{DA} &= -\left(\boldsymbol{R}_1^{0\top 0}\boldsymbol{v}_{AC} + {}^1\boldsymbol{v}_{CD}\right), & {}^1\boldsymbol{v}_{FB} &= -\left(\boldsymbol{R}_1^{0\top 0}\boldsymbol{v}_{BC} + {}^1\boldsymbol{v}_{CF}\right), \\ {}^1\boldsymbol{v}_{FI} &= {}^1\boldsymbol{v}_{FG} + \boldsymbol{R}_2^{12}\boldsymbol{v}_{GI}, & {}^1\boldsymbol{v}_{FH} &= {}^1\boldsymbol{v}_{FG} + \boldsymbol{R}_2^{12}\boldsymbol{v}_{GH}, \\ {}^2\boldsymbol{v}_{HI} &= {}^2\boldsymbol{v}_{GI} - {}^2\boldsymbol{v}_{GH}, & {}^2\boldsymbol{v}_{IF} &= -\left(\boldsymbol{R}_2^{1\top 1}\boldsymbol{v}_{FG} + {}^2\boldsymbol{v}_{GI}\right). \end{aligned} \tag{77}$$

The remaining unit vectors are more easily computed leveraging previous results

$${}^1\boldsymbol{u}_{DE} = -{}^1\boldsymbol{u}_{ED}, \qquad {}^1\boldsymbol{u}_{FJ} = -\boldsymbol{R}_2^{12}\boldsymbol{u}_{JF}, \qquad {}^2\boldsymbol{u}_{HF} = -\boldsymbol{R}_2^{1\top 1}\boldsymbol{u}_{FH}, \qquad {}^2\boldsymbol{u}_{IJ} = -{}^2\boldsymbol{u}_{JI}, \qquad {}^2\boldsymbol{u}_{IH} = -{}^2\boldsymbol{u}_{HI}. \tag{78}$$

Finally, the torque induced on each of the joints by the forces acting on the attachment points is

$$\boldsymbol{\tau}_{\boldsymbol{E}} = \begin{bmatrix} {}^0\boldsymbol{p}_E^\top \boldsymbol{L}_z^\top \boldsymbol{R}_1^0 \\ {}^1\boldsymbol{p}_E^\top \boldsymbol{L}_z^\top \boldsymbol{R}_1^1 \\ \boldsymbol{0} \end{bmatrix} {}^1\boldsymbol{f}_E, \qquad \boldsymbol{\tau}_{\boldsymbol{J}} = \begin{bmatrix} {}^0\boldsymbol{p}_J^\top \boldsymbol{L}_z^\top \boldsymbol{R}_2^0 \\ {}^1\boldsymbol{p}_J^\top \boldsymbol{L}_z^\top \boldsymbol{R}_2^1 \\ {}^2\boldsymbol{p}_J^\top \boldsymbol{L}_z^\top \boldsymbol{R}_2^2 \end{bmatrix} {}^2\boldsymbol{f}_J, \tag{79}$$

whereas the joint torques induced by the forces acting on the spreaders is

$$\boldsymbol{\tau}_{\boldsymbol{D}} = \begin{bmatrix} {}^0\boldsymbol{p}_D^\top \boldsymbol{L}_z^\top \boldsymbol{R}_1^0 \\ {}^1\boldsymbol{p}_D^\top \boldsymbol{L}_z^\top \boldsymbol{R}_1^1 \\ \boldsymbol{0} \end{bmatrix} {}^1\boldsymbol{f}_D, \quad \boldsymbol{\tau}_{\boldsymbol{F}} = \begin{bmatrix} {}^0\boldsymbol{p}_F^\top \boldsymbol{L}_z^\top \boldsymbol{R}_1^0 \\ {}^1\boldsymbol{p}_F^\top \boldsymbol{L}_z^\top \boldsymbol{R}_1^1 \\ \boldsymbol{0} \end{bmatrix} {}^1\boldsymbol{f}_F, \quad \boldsymbol{\tau}_{\boldsymbol{H}} = \begin{bmatrix} {}^0\boldsymbol{p}_H^\top \boldsymbol{L}_z^\top \boldsymbol{R}_2^0 \\ {}^1\boldsymbol{p}_H^\top \boldsymbol{L}_z^\top \boldsymbol{R}_2^1 \\ {}^2\boldsymbol{p}_H^\top \boldsymbol{L}_z^\top \boldsymbol{R}_2^2 \end{bmatrix} {}^2\boldsymbol{f}_H, \quad \boldsymbol{\tau}_{\boldsymbol{I}} = \begin{bmatrix} {}^0\boldsymbol{p}_I^\top \boldsymbol{L}_z^\top \boldsymbol{R}_2^0 \\ {}^1\boldsymbol{p}_I^\top \boldsymbol{L}_z^\top \boldsymbol{R}_2^1 \\ {}^2\boldsymbol{p}_I^\top \boldsymbol{L}_z^\top \boldsymbol{R}_2^2 \end{bmatrix} {}^2\boldsymbol{f}_I. \tag{80}$$

Finally, combine Equations (72), (73), (76), (79), and (80) to arrive at the following expression for the control matrix:

$$\boldsymbol{B} = \begin{bmatrix} \dfrac{\eta_0}{i_0} & \dfrac{\eta_A}{i_A r_A} \displaystyle\sum_{k \in C_{A_1}} {}^0\boldsymbol{p}_k^\top \boldsymbol{L}_z^\top \boldsymbol{R}_1^0 \boldsymbol{c}_k & \dfrac{\eta_B}{i_B r_B} \left(\displaystyle\sum_{k \in C_{B_1}} {}^0\boldsymbol{p}_k^\top \boldsymbol{L}_z^\top \boldsymbol{R}_1^0 \boldsymbol{c}_k + \sum_{k \in C_{B_2}} {}^0\boldsymbol{p}_k^\top \boldsymbol{L}_z^\top \boldsymbol{R}_2^0 \boldsymbol{c}_k \right) \\ 0 & \dfrac{\eta_A}{i_A r_A} \displaystyle\sum_{k \in C_{A_1}} {}^1\boldsymbol{p}_k^\top \boldsymbol{L}_z^\top \boldsymbol{R}_1^1 \boldsymbol{c}_k & \dfrac{\eta_B}{i_B r_B} \left(\displaystyle\sum_{k \in C_{B_1}} {}^1\boldsymbol{p}_k^\top \boldsymbol{L}_z^\top \boldsymbol{R}_1^1 \boldsymbol{c}_k + \sum_{k \in C_{B_2}} {}^1\boldsymbol{p}_k^\top \boldsymbol{L}_z^\top \boldsymbol{R}_2^1 \boldsymbol{c}_k \right) \\ 0 & 0 & \dfrac{\eta_B}{i_B r_B} \displaystyle\sum_{k \in C_{B_2}} {}^2\boldsymbol{p}_k^\top \boldsymbol{L}_z^\top \boldsymbol{R}_2^2 \boldsymbol{c}_k \end{bmatrix}. \tag{81}$$

where $C_{A_1} \coloneqq \{D, E\}$ is the set of all contact points for cable A on the arm; $C_{B_1} \coloneqq \{F\}$ and $C_{B_2} \coloneqq \{H, I, J\}$ are the sets of all contact points for cable B on the arm and forearm, respectively; and vectors $\boldsymbol{c}_k$ are

$$\boldsymbol{c}_E = \begin{cases} {}^1\boldsymbol{u}_{EA}, & \text{if } \theta_1 \geq \theta_1^*, \\ {}^1\boldsymbol{u}_{ED}, & \text{otherwise,} \end{cases} \qquad \boldsymbol{c}_J = \begin{cases} {}^2\boldsymbol{u}_{JF}, & \text{if } \theta_2 \geq \theta_2^*, \\ {}^2\boldsymbol{u}_{JI}, & \text{otherwise,} \end{cases}$$

$$\boldsymbol{c}_D = \begin{cases} \boldsymbol{0}, & \text{if } \theta_1 \geq \theta_1^*, \\ {}^1\boldsymbol{u}_{DA} + {}^1\boldsymbol{u}_{DE}, & \text{otherwise,} \end{cases} \qquad \boldsymbol{c}_F = \begin{cases} {}^1\boldsymbol{u}_{FB} + {}^1\boldsymbol{u}_{FJ}, & \text{if } \theta_2 \geq \theta_2^*, \\ {}^1\boldsymbol{u}_{FB} + {}^1\boldsymbol{u}_{FI}, & \text{if } \theta_2^{**} \leq \theta_2 < \theta_2^*, \\ {}^1\boldsymbol{u}_{FB} + {}^1\boldsymbol{u}_{FH}, & \text{if } \theta_2 < \theta_2^{**}, \end{cases} \tag{82}$$

$$\boldsymbol{c}_H = \begin{cases} \boldsymbol{0}, & \text{if } \theta_2 \geq \theta_2^{**}, \\ {}^2\boldsymbol{u}_{HF} + {}^2\boldsymbol{u}_{HI}, & \text{otherwise,} \end{cases} \qquad \boldsymbol{c}_I = \begin{cases} \boldsymbol{0}, & \text{if } \theta_2 \geq \theta_2^*, \\ {}^2\boldsymbol{u}_{IJ} + {}^2\boldsymbol{u}_{IF}, & \text{if } \theta_2^{**} \leq \theta_2 < \theta_2^*, \\ {}^2\boldsymbol{u}_{IJ} + {}^2\boldsymbol{u}_{IH}, & \text{if } \theta_2 < \theta_2^{**}. \end{cases}$$

Acknowledgments

The authors would like to thank William Doggett for his advice on the intersection of structures, robotics, and in-space assembly and manufacturing; and Joshua Moser and Matthew Vaughan for their comments and suggestions, which have greatly improved the quality of the paper.

References

[1] Wong, I. M., and Cline, J. E., "LSMS–L35, Miniature Crane for Payload Off-loading and Manipulation: Development, and Application," *ASCEND*, Las Vegas, NV, USA, 2022, pp. 1–17. https://doi.org/10.2514/6.2022-4237.

[2] Grande, M. L., Moses, R. W., Cosgrove, P. A., Mueller, R. P., Prater, T. J., and Blanchard, A. J., "Protecting Crew and Surface Systems with a Long-Duration Lunar Safe Haven," *ASCEND*, Las Vegas, NV, USA, 2021, pp. 1–14. https://doi.org/10.2514/6.2021-4070.

[3] Dorsey, J., Jones, T., Doggett, W., King, B., Mercer, C., Brady, J., Berry, F., Anderson, E., and Ganoe, G., "Recent Developments in the Design, Capabilities and Autonomous Operations of a Lightweight Surface Manipulation System and Testbed," *AIAA SPACE Conference & Exposition*, Long Beach, CA, USA, 2011, pp. 1–20. https://doi.org/10.2514/6.2011-7266.

[4] Doggett, W., Dorsey, J., Collins, T., King, B., and Mikulas, M., "A Versatile Lifting Device for Lunar Surface Payload Handling, Inspection & Regolith Transport Operations," *American Institue of Physics Conference Proceedings*, Vol. 969, No. 1, 2008, pp. 792–808. https://doi.org/10.1063/1.2845045.

[5] *Peregrine Lunar Lander, payload user's guide*, Astrobotics, Pittsburg, PA, USA, 2023. URL https://www.astrobotic.com/lunar-delivery/landers/peregrine-lander/, visited on 02/02/2024.

[6] Blue Origin, "Blue Moon, Lunar Landers," , 2007-2023. URL https://www.blueorigin.com/blue-moon, visited on 02/02/2024.

[7] Angeles, J., *Fundamentals of Robotic Mechanical Systems, Theory, Methods, and Algorithms*, 4^{th} ed., Springer, Switzerland, 2014.

[8] Donald, B. R., Xavier, P. G., Canny, J. F., and Reif, J. H., "Kinodynamic motion planning," *Journal of the ACM*, Vol. 40, No. 5, 1993, pp. 1048–1066.

[9] Puig-Navarro, J., Bisio, D. R., Pye, J. E., Granov, Y., Moser, J. N., Friz, J. S., Waltz, W. J., Cline, J. E., and Allen, B. D., "A Trajectory Tracking Algorithm for the LSMS Family of Cable-Driven Cranes," *Robotics: Science and Systems (RSS)*, Delft, The Netherlands, 2024, pp. 1–12.

[10] Ginsberg, J., *Engineering Dynamics*, Cambridge University Press, New York, NY, USA, 2008.

[11] Ehmann, S. A., and Lin, M. C., "Accurate and Fast Proximity Queries Between Polyhedra Using Convex Surface Decomposition," *Computer Graphics Forum*, Vol. 20, No. 3, 2002, pp. 500–511.

[12] Dorsey, J., Mikulas, M., and Doggett, W., "Preliminary Structural Design Considerations and Mass Efficiencies for Lunar Surface Manipulator Concepts," *AIAA SPACE Conference & Exposition*, San Diego, CA, USA, 2008, pp. 1–17. https://doi.org/10.2514/6.2008-7916.